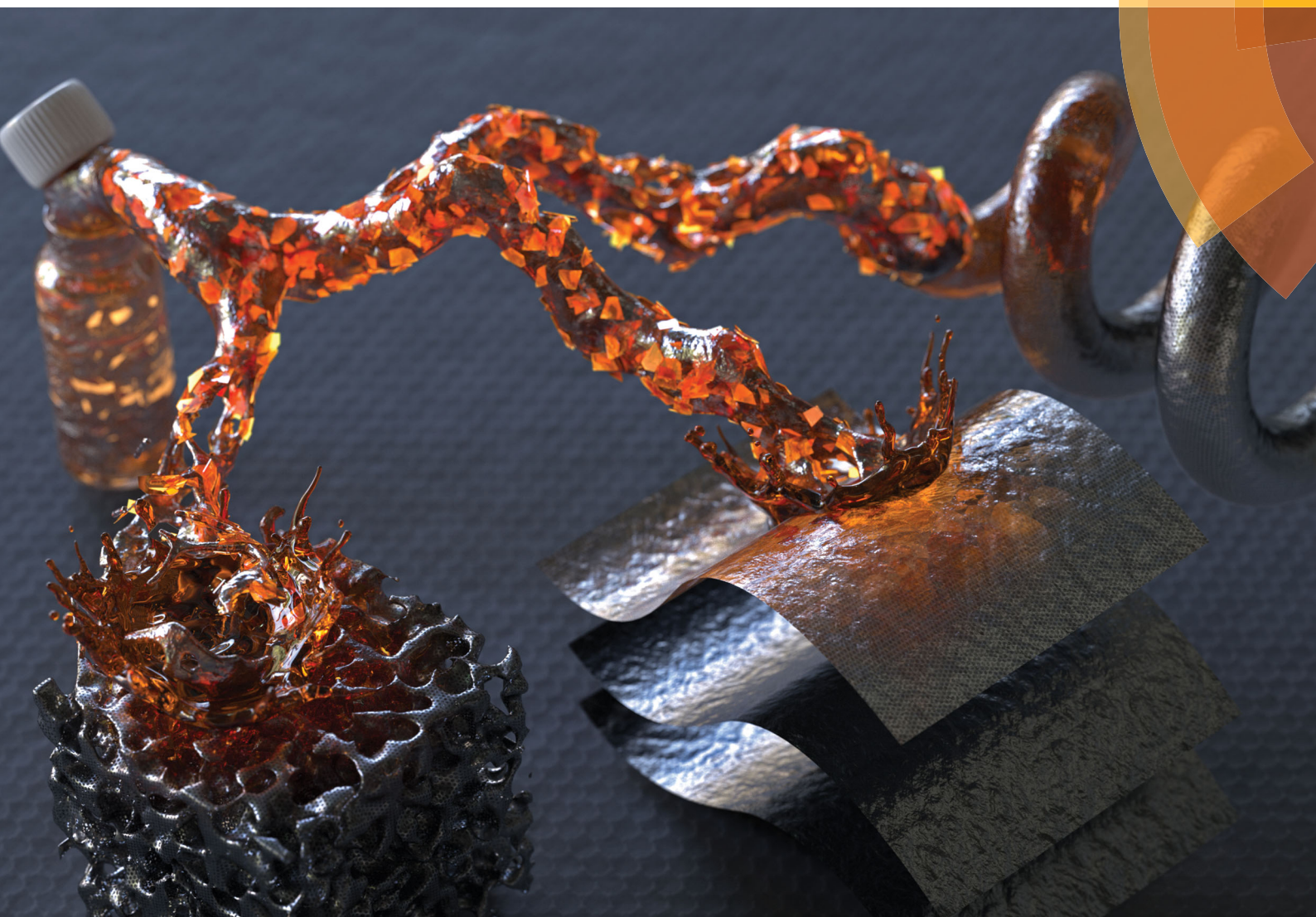


Chem Soc Rev

Chemical Society Reviews

rsc.li/chem-soc-rev



Themed issue: 2D nanomaterials: beyond graphene and transition metal dichalcogenides

ISSN 0306-0012



ROYAL SOCIETY
OF CHEMISTRY

REVIEW ARTICLE

Tae Hee Han, Sang Ouk Kim *et al.*
Graphene oxide liquid crystals: a frontier 2D soft material for
graphene-based functional materials



Cite this: *Chem. Soc. Rev.*, 2018, 47, 6013

Graphene oxide liquid crystals: a frontier 2D soft material for graphene-based functional materials

Suchithra Padmajan Sasikala,^{†a} Joonwon Lim,^{†a} In Ho Kim,^{†a} Hong Ju Jung,^{†a} Taeyong Yun,^{†a} Tae Hee Han,^{†b} and Sang Ouk Kim^{†a*}

Graphene, despite being the best known strong and electrical/thermal conductive material, has found limited success in practical applications, mostly due to difficulties in the formation of desired large-scale highly organized structures. Our discovery of a liquid crystalline phase formation in graphene oxide dispersion has enabled a broad spectrum of highly aligned graphene-based structures, including films, fibers, membranes, and mesoscale structures. In this review, the current understanding of the structure–property relationship of graphene oxide liquid crystals (GOLCs) is overviewed. Various synthetic methods and parameters that can be optimized for GOLC phase formation are highlighted. Along with the results from different characterization methods for the identification of the GOLC phases, the typical characteristics of different types of GOLC phases introduced so far, including nematic, lamellar and chiral phases, are carefully discussed. Finally, various interesting applications of GOLCs are outlined together with the future prospects for their further developments.

Received 16th April 2018

DOI: 10.1039/c8cs00299a

rsc.li/chem-soc-rev

^a National Creative Research Initiative Centre for Multi-Dimensional Directed Nanoscale Assembly, Department of Materials Science & Engineering, KAIST, Daejeon 34141, Republic of Korea. E-mail: sangouk@kaist.ac.kr

^b Department of Organic and Nano Engineering, Hanyang University, Seoul 04763, Republic of Korea. E-mail: than@hanyang.ac.kr

[†] Equal contribution.

1. Introduction

The emergence of graphene has led to intensive research yielding a wealth of knowledge on novel two-dimensional (2D) platforms of materials and devices over the past decade. Given the outstanding electrical, thermal, mechanical, and other physical properties of graphene, nonetheless graphene is yet



Suchithra Padmajan Sasikala

Suchithra Padmajan Sasikala received her PhD degree in Chemistry as a CSIR senior research fellow from the University of Kerala (India) in 2011. She carried out CSIR-Nehru Science Postdoctoral Fellowship at the National Institute of Science and Technology (India) from 2011–2013. She also worked as a visiting scientist at UHasselt (Belgium) in 2012. She carried out postdoctoral work under the Initiative of Excellence (IdEx) program at the University of Bordeaux, (France) in the period of 2013–2015. She joined Prof. Sang Ouk Kim's soft nanomaterials group in KAIST (South Korea) as a postdoctoral fellow in 2016. She is currently working as a research assistant professor (KAIST) and her current research interest is mainly focused on the liquid crystal processing of graphene fiber and other two-dimensional materials.



Joonwon Lim

Joonwon Lim received his BE degree in Information Display from Kyung Hee university (South Korea) in 2008. He completed his dual MS degrees in Information Display from Kyung Hee University and Sciences et Technologies from Ecole Polytechnique (France) in 2011. He received his PhD degree from KAIST (South Korea) under the supervision of Prof. Sang Ouk Kim in 2016. From 2016 to 2017, he worked as a postdoctoral fellow in the same group. He is currently working as a professional researcher in LG Chemistry. His current research interest is focused on the synthesis of functional nanomaterials and their applications in energy, the environment, sensors, etc.

to be widely used in many real-world commercial applications. This is largely due to the notoriously difficult processing demands for high-performance graphene-based materials and devices. In general, a large-scale market application of novel nanomaterials commonly relies on a high solution dispersibility and processability. Unfortunately, many nanoscale materials, including pristine graphene, suffer from a generic low solvent dispersibility, arising from their low entropy gain for mixing, which is clearly in contrast to many common small molecular species with genuinely high mixing entropy. Along the same vein, the promise of graphene and other 2D materials could be fulfilled if we could develop reliable methodologies to manipulate them in a highly dispersed solution state to suit the specific requirements for different applications.

Our world-first discovery of the liquid crystalline phase in aqueous dispersions of graphene oxide (GO) in 2009 is remarkably significant in this context as it provides an unprecedented handle to align, manipulate, and process 2D graphene-based materials in a large scale in a specifically customizable manner.^{1–13} It is noteworthy that liquid crystal (LC) phase formation is a general behavior for any kind of molecules or particles with a sufficient degree of shape anisotropy, while they are uniformly dispersed in space (with or without a solvent) under the influence of thermal fluctuation. Unlike the typical synthetic methods for GO, such as Hummers method, which yields excessive acidic and other ionic impurities, the emergence of a LC phase from GO dispersions generally requires the sufficient removal of those ionic impurities for the thermodynamically stabilized colloidal dispersibility. Once such a colloidal stability is attained, the inherent molecular order of the LC phase can be maneuvered for a variety of multi-dimensional functional structures.^{6,8,11,14} In contrast to the conventional small molecular LCs, however,

GOLCs are very unique in terms of their extremely large shape anisotropy of the mesogenic units along with other unusual features, such as a large polydispersity in the size and shape of mesogens, which may cause difficulties in the precise control of the LC alignment over an arbitrary long range. Nonetheless, a wide range of application fields, ranging from structural materials, to electrical/thermal materials, separation media, energy storage/conversion, catalysis, and model display technologies, have already been demonstrated exploiting the spontaneous ordering in GOLCs.^{12,13,15,16} As our fundamental understanding of GOLCs grow, this novel field of science should deliver more opportunities in various application fields in the near future.

The aim of this review is to offer fundamental insights into the structure and properties of GOLCs and to promote their further development aiming at real-world applications. It is noteworthy that there are quite a few review articles already available for GOLCs, including ours.^{17–20} In this review, we tried to avoid an overlap with the previous ones and to include recent new ideas and concepts as well as to propose novel viewpoints and insights. We specifically focus on the methodologies for the still-challenging synthesis and structural characterization methods for GOLCs. Different aspects of the available synthetic strategies are highlighted that are frequently overlooked in the preparation of GOLCs. The properties and application fields of GOLCs with many interesting examples are also discussed. Finally, some conclusions and our outlook outline the broad prospects in this field, including the latest advances and relevant potential challenges. Our expectation is also proposed for the potential real-world practical accomplishment in the near future.



Tae Hee Han

Tae Hee Han is an associate professor in the Department of Organic and Nano Engineering at Hanyang University and a group leader in the Hybrid Functional Nano Materials Laboratory, Seoul, Korea, since 2012. He obtained his PhD under Prof. Sang Ouk Kim at the Department of Materials Science and Engineering at KAIST in 2010 and was a postdoctoral fellow in Prof. Jiaixng Huang's group at the Department of Materials Science

and Engineering at Northwestern University until 2012. His main research interest is focused on the fundamental understanding of colloidal properties of soft 2-dimensional nanomaterials and their liquid crystalline assembly-based nano-architectonics.



Sang Ouk Kim

Sang Ouk Kim is a professor in the Department of Materials Science and Engineering at KAIST, and a director of the National Creative Research Initiative Center for Multi-Dimensional Directed Nanoscale Assembly and Graphene Liquid Crystalline Fiber Center, Daejeon, Korea. He obtained his PhD at KAIST in 2000 and performed postdoctoral research at the University of Wisconsin-Madison, USA. Prof. Kim has published more than 200 SCI

journal papers and delivered more than 300 invited presentations thus far. He is the recipient of numerous prestigious awards and is serving as an associate editor for Energy Storage Materials and on the editorial board of many scientific journals. Prof. Kim's research group is actively researching the nanoscale assembly and chemical modification of various nanomaterials, including graphene-based materials. His group discovered the graphene oxide liquid crystal in 2009.

2. Liquid crystallinity in nanomaterials: general overview

In this section, an outline of liquid crystallinity is briefly introduced in order to acquaint the readers with the basic scientific understanding of LC systems. The LC phase is the a truly thermodynamically stable state of matter succeeding the traditionally well-defined solid, liquid, and gas phases. All these different phases are characterized by the different degrees of atomic or molecular ordering. For instance, a crystalline solid is characterized by long-range 3D atomic order, whereas a liquid has a short-range order and a gas has a completely disordered structure. A LC phase is generally intermediate between the typical solid and liquid phases in terms of molecular ordering and relevant properties, so that it is often called a mesophase (literally meaning middle shape). A material in the LC phase synergically combines the characteristics of both a solid (anisotropy/orientational order) and a liquid (fluid property/collective mobility), and hence is also termed as an anisotropic fluid. Such materials exhibit interesting rheological properties intermediate between typical solids and liquids, as well as exciting optical, mechanical, viscoelastic, and dielectric properties.

Since Reinitzer discovered the optical birefringence of cholesterol in 1888, the study of LC materials has gradually evolved over the proceeding century so that we can now frequently encounter LC materials in both natural systems and many application fields.²¹ Generally, LC phase formation can be understood from the viewpoint of either purely entropic driving forces driven by the excessive degree of freedom for translational ordering (Onsager theory) or enthalpic attractive intermolecular interactions (Maier-Saupe theory), both of which can overcome the entropic penalty for the molecular alignment (loss of rotational degree of freedom) in LC states.^{22,23} It is noteworthy that without net attractive interactions among GO platelets (in fact, GO platelets repulse each other as they are negatively charged due to the deprotonated oxygen functional groups at their surfaces), Onsager theory should be more appropriate for the description of GOLC behavior.

There are many different classification methods for LCs, including the widely used LC phase transition evolution condition. The LC phase can be induced either by a temperature change in the pristine form (thermotropic LC phases) or by a concentration change in the solution state (lyotropic LC phases). The constituent units of the LC phase are often called mesogens, based on the anisotropic structures, of which the LC materials can be classified into calamitic (rod-like), discotic (disk-like), and banana (bent) LCs. The aspect ratio in the anisotropic shape as well as the geometry and orientation of the mesogens dominate the phase structures of the LC phase as a whole, on the basis of which, LC phases can be classified into nematic (mesogens uniaxially aligned without positional order), smectic (mesogens showing 1D positional ordering with layered structures), and cholesteric (also called chiral nematic with a helical arrangement of mesogens through the chiral axis). Interestingly, one can obtain a cholesteric LC by introducing a nematic LC with chiral additives or dopants.²⁴ A schematic representation for the general LC classifications together with the structures of the representative mesogens is given in Fig. 1.

LCs are widely used in many different functional materials and devices. For instance, small molecular LCs are vital for modern information display technology (*i.e.*, LCDs) for mobile devices to large-area television screens and also in telecommunications, photonics, drug delivery, optical lens, chemical and biological sensors, and so on. Polymeric LCs are more specifically useful for high-performance material processing, including the wet-spinning of super-strong LC fibers (Aramid fibers) and for the injection molding of strong bulk materials. To date, various aspects of LCs have been widely reviewed.^{25–32} Thus, all the different LC materials, other than GOLCs, but including natural and synthetic small molecular or polymer LCs, are beyond the scope of this article. Instead, typical LCs based on organic or inorganic nanostructured materials are briefly summarized below.

The organization of nanomaterials into ordered structures is a general requirement for a wide spectrum of materials and device applications. In this regard, the synergic integration of functional nanomaterials with LC ordering is an intriguing idea that has been broadly investigated in the field of nanoscience and nanotechnology. Sufficiently small nanoparticles commonly do not influence the LC phase formation but are able to endow new functionalities. Concurrently, disordered nanomaterials may benefit from the long-range order of LCs and can align themselves to form ordered functional structures. Au nanoparticles are a typical popular nanomaterial widely exploited in both lyotropic and thermotropic LC hosts (*i.e.*, thiol-based organic mesogens). In particular, an interesting subject to investigate is the spontaneous formation of ordered Au arrays under the geometric confinement enforced by LC ordering. The incorporation of Au components has been found to improve the electro-optical response of a LC host, which may have potential impact on current display technology regarding potentially a lower operating voltage, higher image contrast, and faster switching speed.³¹ Similarly, other metallic (Pd, Ag), semiconductor (CdS, CdSe, TiO₂, Sn₂P₂S₆, BaTiO₃), inorganic oxide (MgO, SiO₂), magnetic (Ni, Fe₃O₄) and carbon-based (CNT, fullerene) nanomaterials have been found to offer significant advantages to LC properties, such as optical, optoelectronic, surface plasmon resonance, magnetic susceptibility, and memory effects and also on the realization of metamaterials.^{33–35} The possibility of lyotropic colloidal LC phase formation can be perceived for the solvent dispersions of anisotropic nanomaterials without any host LC phase. For instance, nanomaterials having 1D nanorod/wire/tube and 2D disk/sheet morphologies have geometrical anisotropy (calamitic and discotic, respectively) that can induce LC phases while dispersed in a suitable solvent at a sufficiently high concentration. A wide range of nanomaterials, including of metallic, semiconducting, biological, and pharmaceutical origin, have been identified as LCs with nematic, smectic, lamellar, and hexagonal mesophases (Table 1). Among these, high-aspect-ratio gold nanorods, clay minerals, CNTs and GO LCs have been extensively investigated to exploit their outstanding mechanical, electrical, optical, sensing, thermal, and antimicrobial properties. The list is not at all exhaustive since research on anisotropic nanomaterials of organic and

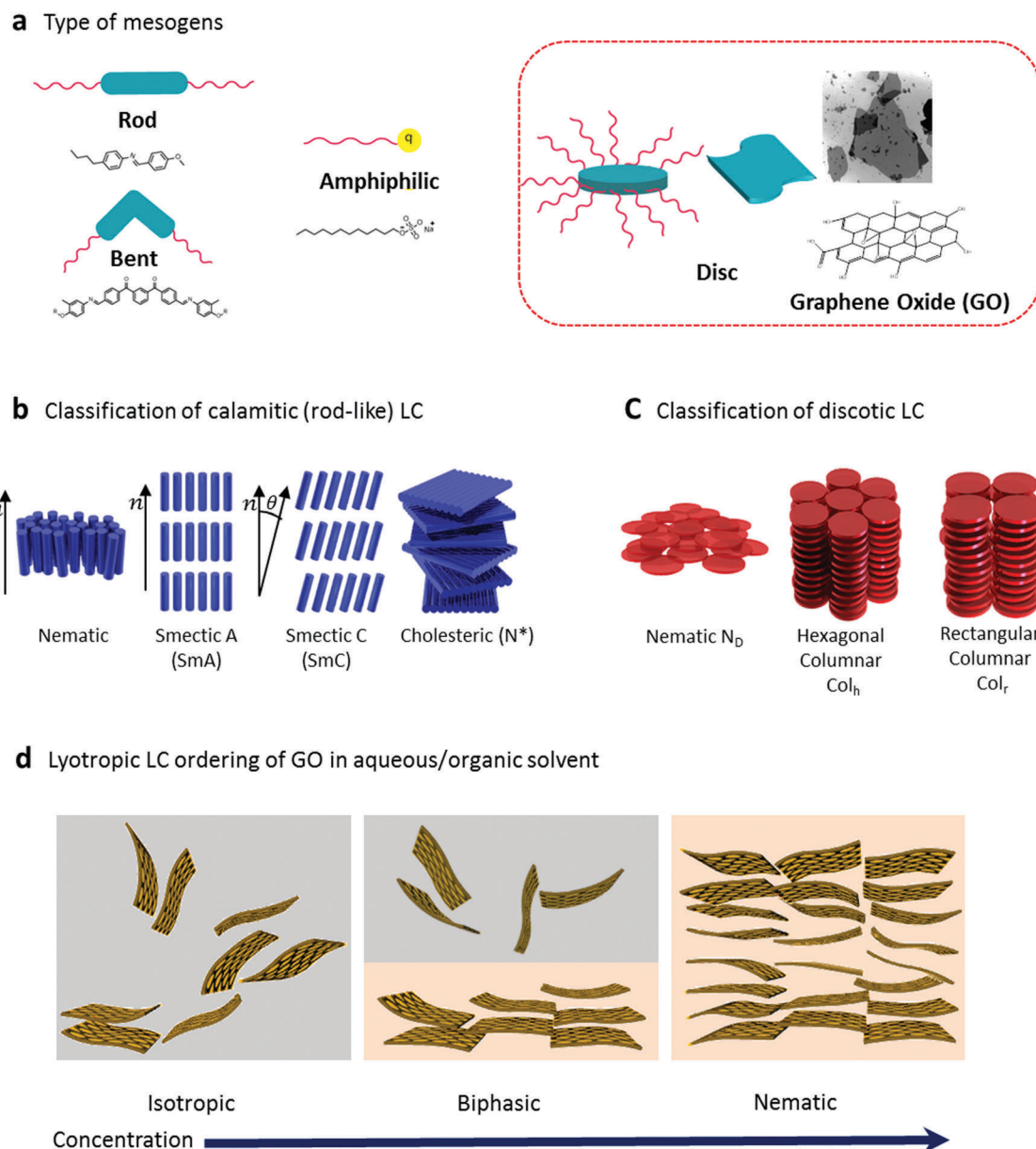


Fig. 1 Different classification of LC materials: (a) typical examples of mesogens with different molecular shapes forming LC phases. GO comes under the discotic shape category. SEM picture of a GO sheet is provided in the inset. (b and c) Classification based on the orientation of mesogens, (d) Schematic representing the isotropic to nematic phase transition of a GO dispersion with increasing concentration.

Table 1 Nanoscale materials showing liquid crystallinity

Type	Description	Ref.
Clay (2D)	Bentonite (montmorillonite), saponite, nontronite, laponite, imogolite	138–142
2D inorganics	Phosphoantimonate ($\text{H}_3\text{Sb}_3\text{P}_2\text{O}_{14}$), $\text{Ni}(\text{OH})_2$, gibbsite ($\text{Al}(\text{OH})_3$), $\text{Co}(\text{OH})_2$, CuS , GdF_3 , layered double hydroxides (Mg, Al-LDH)	143–149
2D graphene derivatives	Graphene, graphite oxide, graphene oxide, reduced graphene oxide	38 and 40–42
2D transition metal dichalcogenides	MoS_2	43
2D carbides (MXene)	$\text{Ti}_3\text{C}_2\text{Tx}$	185
Inorganic metal, metal oxides, and semiconductors, (1D rod)	Gold nanorods(GNR), geothite (FeOOH), boehmite (AlOOH), lanthanum phosphate (LaPO_4), SiO_2 , V_2O_5 , ZnO , TiO_2 , SnO_2 , CdTe , CdSe	88 and 150–159
Inorganic nanowires (1D)	Ag, ZnO	160 and 161
Nanotubes (1D)	MWCNT, SWCNT	162–164
Biological	Tobacco mosaic virus, DNA, cellulose, peptide	165–168
Pharmaceuticals	Fenoprofen, folic acid, nafcillin, methotrexate	169

inorganic nature showing lyotropic LC behavior remains a hot topic. Additionally, LC ordering has also been frequently observed for a broad range of anisotropic nanoparticles at the air–water interface (Langmuir–Blodgett films) and in evaporated films. Interested readers are suggested to refer to the available detailed reviews on the topic.^{36,37}

3. Graphene oxide liquid crystals (GOLCs)

3.1. History of GOLCs: discovery and milestones

In 2009, we first discovered that GO could exhibit LC behavior in aqueous media with typical nematic ordering.^{1–4} As such, GOLCs can be considered as a general category of lyotropic colloidal LCs. This discovery was reconfirmed by Gao *et al.* and many others worldwide, where the collective scientific efforts of many researchers have contributed to a greater recent general understanding of the typical physical behaviors of GOLCs.^{6,7,38} The possibility of a highly aligned state enabled by the spontaneous molecular ordering in the LC phase has triggered many interesting potential material and device applications of GOLCs. It is noteworthy that, while the discovery of other carbon-based LCs, such as carbon nanotube LCs (CNTLCs), predates our discovery of GOLCs, many reports on the relevant works, including graphene LCs (GLCs), reduced graphene oxide LCs (rGOLCs), and graphite oxide LCs (GtOLCs), succeeded our initial discovery (Fig. 2).^{39–42} GOLCs have been widely popularized and many direct and parallel applications were developed in a relatively short span of time due to their simple and straightforward synthetic route. Moreover, the wide popularity of GOLCs has also triggered the discovery of other two-dimensional LC systems, such as MoS₂ and Mxene.^{43,185}

While the principal constituent elements (mesogens) in GOLCs are GO sheets, many parameters, such as the shape anisotropy and polydispersity of GO, ionic strength, mass/volume fraction, and pH value, can influence the LC phase behavior. In addition, it is also necessary to understand the procedures for the size-controlled

synthesis of GO. For this reason, the following subsections are dedicated to acquaint the readers with the synthesis methods that have been developed for GO, together with an insight into the GO structure. We will further explain the mechanism and influencing factors for the GOLC formation, followed by the general characterization methods and properties of GOLCs.

3.2. Synthesis of graphene oxide (GO)

Analogous to the exfoliation of graphene from graphite, GO can be exfoliated from graphite oxide. The history of graphite oxide dates back more than 150 years. Brodie first reported the synthesis of graphite oxide from pristine graphite in 1859.⁴⁴ By contrast, the synthesis of graphite oxide has been activated only in the last decade, principally motivated from the pioneering contribution by Ruoff *et al.*^{45–47} Several well-known methods are listed in Table 2. Notably among these, modified Hummers methods are the most widely employed, particularly for the industrial production of GO while ensuring scalability and high yield.^{48–53} Nevertheless, such chemical oxidation methods have an intrinsic limitation associated with an explosive risk from the permanganate oxidant. This issue can be partly addressed by utilizing relatively safer oxidizing methods with mild chemicals, such as K₂FeO₄, or electrochemical water oxidation (Fig. 3).^{54,55} Such wet-chemical/electrochemical oxidation methods were further developed to achieve a maximum carbon-to-oxygen (C/O) ratio of between 2.0 and 2.9.⁵⁵ Note that these reported (C/O) ratios may not always be reliable due to the strong hygroscopic nature and nonstoichiometric composition of graphite oxide.⁵⁶ According to the Lerf–Klinowski model of graphite oxide established in 1998 (Fig. 4a), three types of oxygen functional groups, namely epoxy (on the carbon plane), hydroxyl and carboxyl groups (above and below the carbon plane), can be introduced into the graphite structure.^{57,58} This structure suggests that epoxide groups in the planar carbon lattice are chemically inactive due to the negatively charged oxygen layers preventing nucleophilic attack.⁵⁷ Gao and Ajayan *et al.*⁵⁹ improvised this model, stating

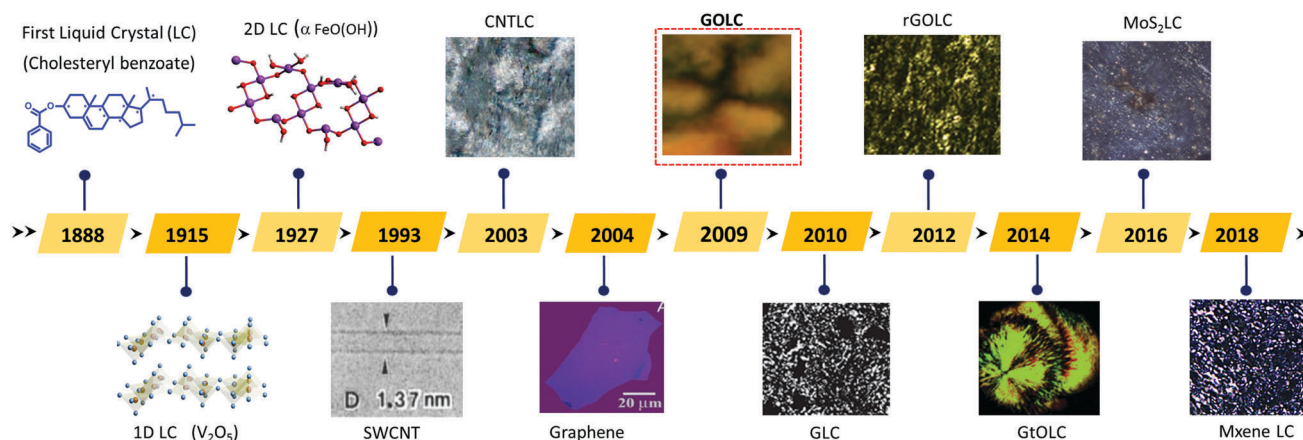


Fig. 2 Timeline displaying the discovery of LCs from 1D to 2D mesogens.^{2,21,40–43,159,162,178,185} Discovery of CNT and graphene are also included in the timeline.^{179–181} Reproduced from ref. 2 with permission from John Wiley and Sons, copyright 2011; reproduced from ref. 179, 40 and 185 with permission from Springer Nature, copyright 1993, 2010, and 2018; reproduced from ref. 41 with permission from the American Chemical Society, copyright 2012, reproduced from ref. 162 and 181 with permission from the American Association for the Advancement of Science, copyright 2003 and 2004.

Table 2 Different synthesis protocols of GO

Name	Year	Oxidizing agents/steps	C/O ratio*	Advantages	Disadvantages
Brodie method ⁴⁴	1859	KClO ₃ + con. HNO ₃ , 60 °C for 4 days	1.6	The very first synthetic method for graphite oxide	Requirement of four repetitions of the oxidation steps Production of toxic gas (NO ₂ , N ₂ O ₄ , and explosive ClO ₂) Production of toxic gases
Staudenmaier method ¹⁷⁰	1898	KClO ₃ (in small quantities through several steps over the course of reaction) + con. HNO ₃ + con. H ₂ SO ₄	1.6	Convenient and time saving compared to Brodie method	Production of toxic gases (NO _x) Production of toxic gases (NO _x)
Hofmann ¹⁷¹	1937	Same as Staudenmaier method, but with non-fuming HNO ₃		Avoid the usage of corrosive fuming HNO ₃	
Hummers and Offeman ⁴⁹	1958	Graphite treated with NaNO ₃ + KMnO ₄ , <45 °C, 2 h	2.1	Avoid the usage of corrosive fuming HNO ₃	Production of toxic gases (NO _x)
Kovtyukhova <i>et al.</i> ⁴⁸	1999	(i) Con. H ₂ SO ₄ + K ₂ S ₂ O ₈ , P ₂ O ₅ , 80 °C, 6 h (ii) Con. H ₂ SO ₄ + KMnO ₄ , 35 °C, 2 h (iii) 30% H ₂ O ₂ followed by purification	1.3	High level of oxidation	Multiple steps Production of toxic gases (NO _x)
Modified Hummers method by Hirata <i>et al.</i> ¹⁷²	2004	(i) NaNO ₃ + con. H ₂ SO ₄ + KMnO ₄ , 20 °C, 5 days (ii) 30% H ₂ O ₂ followed by purification		High yield compared to Hummers method	Long oxidation reaction Production of toxic gases (NO _x)
Ang and Loh <i>et al.</i> ¹⁷³	2009	(i) NaNO ₃ + con. H ₂ SO ₄ + KMnO ₄ , 90 °C, 0.5 h (ii) Redisperse in DMF + tetrabutyl ammonium hydroxide + H ₂ O, 90 °C, 2 days		High graphene content >90% monolayer	Mild oxidation, long duration, multiple steps
Improved method by Marciano and Tour <i>et al.</i> ^{50,174}	2010	KMnO ₄ + 9 : 1 mixture of con. H ₂ SO ₄ + H ₃ PO ₄ , 50 °C, 12 h. After cooling, reaction mixture treated with 30% H ₂ O ₂ followed by purification		High yield, no toxic gas evolution	Reactive Mn ₂ O ₇ intermediates can cause severe explosion at elevated temperatures
Eigler <i>et al.</i> ¹⁷⁵	2013	NaNO ₃ + con. H ₂ SO ₄ + KMnO ₄ at 30 °C for 21 h. After cooling, reaction mixture treated with 3% H ₂ O ₂ followed by purification		Slow reaction, hence minimum CO ₂ formation	Production of toxic gases (NO _x)
Peng-Gao <i>et al.</i> ⁵⁴	2015	K ₂ FeO ₄ + con. H ₂ SO ₄ , room temperature, 1 h	2.2	Slow and minimum oxidation preserve the carbon lattice	Low yield
Yu-Xing <i>et al.</i> ¹⁷⁶	2016	(i) K ₂ FeO ₄ + KMnO ₄ + H ₃ BO ₃ + con. H ₂ SO ₄ , 35–95 °C, >3 h (ii) 30% H ₂ O ₂	1.9	High yield Mn ion contamination can be avoided. Time of reaction is short and scalable Free of toxic gas (NO _x)	Possibility of Fe contamination. Handling difficulty and pollution associated with con. H ₂ SO ₄ Possibility of Mn, Fe contamination, Handling difficulty and pollution associated with strong acids/oxidants Reactive Mn ₂ O ₇ intermediates can cause severe explosion at elevated temperatures
Yuan-Chen <i>et al.</i> ¹⁷⁷	2017	KMnO ₄ + 9 : 1 mixture of con. H ₂ SO ₄ + H ₃ PO ₄ , 50 °C, ultrasonicated for 3 h. After cooling reaction mixture treated with 30% H ₂ O ₂ followed by purification		Fast reaction. Increased amount of edge carboxyl groups.	Reactive Mn ₂ O ₇ intermediates can cause severe explosion at elevated temperatures
Pei-Ren <i>et al.</i> ⁵⁵	2018	(i) Electrochemical intercalation of graphite with con. H ₂ SO ₄ (ii) After purification electrochemical oxidation with dil. H ₂ SO ₄	1.5	First electrochemical method for synthesis of GO No metal ion contamination. Hence purification is much easier Time of reaction is short	Handling difficulty and pollution associated with con. H ₂ SO ₄ Intrinsic inscalability associated with electrochemical reaction compared to wet-chemical methods

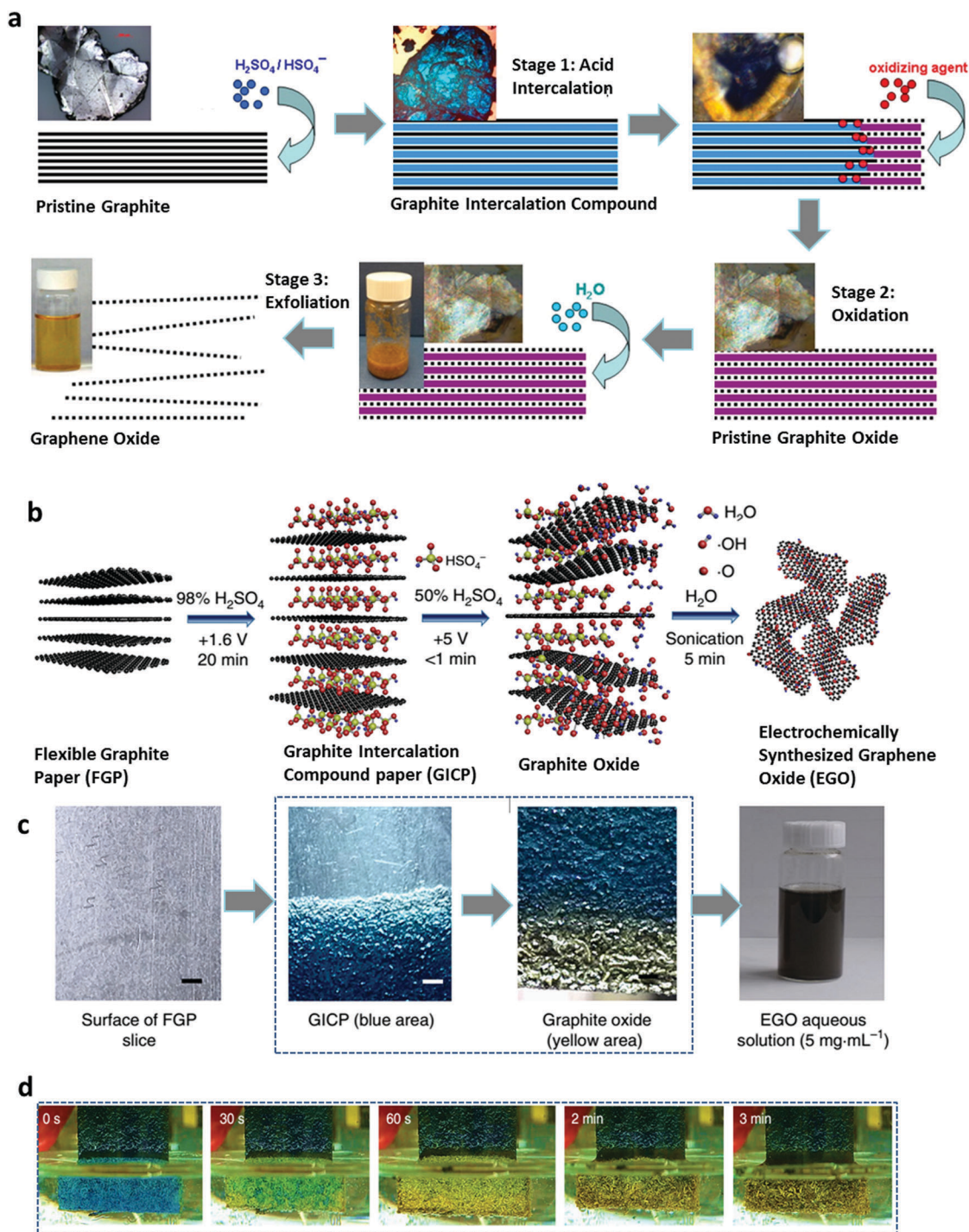


Fig. 3 (a) Schematic representation of the synthesis of GO from pristine graphite using strong chemical oxidants; solid black line and dotted black line represent a single layer of graphene and GO, respectively, while wide blue line and purple line represent an intercalated acid layer and mixture of acid with the reduced form of oxidizing agent, respectively. As shown, three consecutive steps are involved in the synthesis of GO, namely (i) acid intercalation, (ii) oxidation, and (iii) hydrolysis and exfoliation. Optical images of a sample on these synthesis phases are given in the inset. Reproduced from ref. 60 with permission from the American Chemical Society, copyright 2014 (<https://pubs.acs.org/doi/abs/10.1021/nn500606a>). (b) Schematic representation of the synthesis of GO by the water electrolytic oxidation of a commercial flexible graphite paper (FGP). (c) Corresponding photographs of the samples at each stage of the synthesis process, and (d) the boxed area in 'c' is elaborated with real-time photographs of the electrochemical oxidation reaction of GICP (blue colored) to form graphite oxide (yellow colored) within seconds; reproduced from ref. 55 with permission from Nature Communications, copyright 2018 (<http://creativecommons.org/licenses/by/4.0/>).

that graphite oxide consists of five- and six-membered lactol rings, an ester of a tertiary alcohol, hydroxyl, epoxy, and ketone functionalities (Fig. 4b).

As with the case of the structure, the oxidation mechanism of graphite is also controversial. Dimiev and Tour, with the aid of optical microscopy, Raman spectroscopy, and X-ray

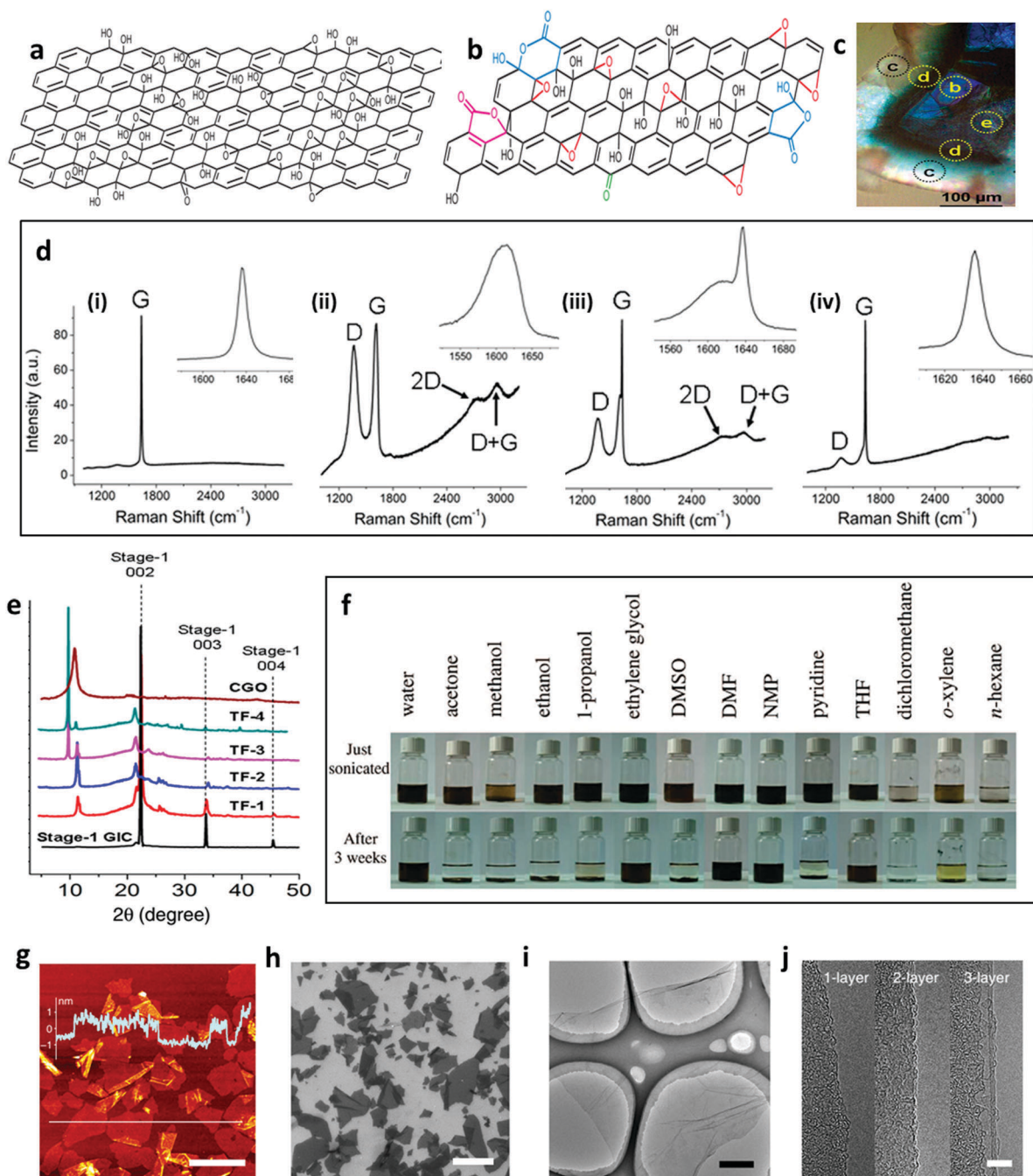


Fig. 4 Chemical structural model of graphite oxide by (a) Lerf–Klinowski, reproduced from ref. 57 with permission from Elsevier, copyright 1998. (b) Gao and Ajayan *et al.* updated model, reproduced from ref. 59 with permission from Springer Nature, copyright 2009. (c) Optical image of a partially oxidized graphite flake retrieved as an intermediate product from the oxidation step. (d) Raman spectra at an excitation wavelength of 514 nm (i, ii, iii, iv) corresponding to spots (b, c, d, and e), respectively in the optical image (c), indicating that the edges are more oxidized than the center. The elevated D band in the Raman spectra indicate the oxidation and defects in the graphene crystal lattice, while the blue shifting of G band (magnified in the inset) indicate charging of the graphene layers by the intercalates. (e) X ray diffraction patterns of different stages of the oxidation reaction of graphite, starting from a graphite intercalation compound (GIC, dark colored spectrum). TF-1 to TF-4 indicates 1 to 4 equivalents of KMnO_4 -treated GIC, while CGO represents the spectrum of graphite oxide (CGO, brown colored spectrum). Reproduced from ref. 60 with permission from American Chemical Society, copyright 2014 (<https://pubs.acs.org/doi/abs/10.1021/nn500606a>). (f) Photograph of graphite oxide directly exfoliated in water and organic solvents by 1 h of ultrasonication (top row) and the stability of GO dispersions after 3 weeks (bottom row), reproduced from ref. 61 with permission from the American Chemical Society, copyright 2008. (g–j) typical microscopic characterization of GO: (g) atomic force microscopy (AFM), (h) scanning electron microscopy (SEM), (i) transmission electron microscopy (TEM), and (j) high-resolution TEM (HRTEM) images of GO sheets synthesized by electrolytic water oxidation method. Reproduced from ref. 55 with permission from Nature Communications, copyright 2018 (<http://creativecommons.org/licenses/by/4.0/>).

diffraction (XRD), reported a reliable model, where the rate-determining step of oxidation involved the diffusion of oxidizing agents into the graphite interlayers during the synthesis of GO.⁶⁰ They implied that the oxidation reaction can be stopped at any stage of the reaction and the intermediate products can be recovered and stored. For instance, Fig. 4c shows an optical image of partially oxidized graphite flakes. The Raman spectra of different points demonstrate that the deep blue colored central part is an unoxidized part and the light yellow colored edges are oxidized parts, supporting the diffusion-controlled oxidation model (Fig. 4d). The sulfate and oxygen functional groups in the graphite interlayers increase the interlayer spacing after oxidation, as evidenced by the XRD studies (Fig. 4e). Accordingly, van der Waals interaction can be diminished between the graphene layers and the graphite oxide can be readily exfoliated into GO sheets (few layers to monolayer) by subsequent mechanical shaking or ultrasonication in water or other polar solvents, such as DMF, DMSO, or NMP (Fig. 4f).⁶¹ Centrifugation procedures can then readily remove the unexfoliated chunk and few-layer GOs effectively to attain monolayer-dominant GO sheets (Fig. 4g–j).

3.2.1. Factors influencing the size of GO. The size of GO sheets can range from 40 nm to 250 μm depending on the precursor graphite source, the employed oxidation method and ultrasonication or shaking condition.^{51,62–65} Graphite precursors with low crystallinity have weak interlayer interaction and hence the oxidants can easily diffuse into the interlayers, leading to an increased interlayer spacing. Similarly, graphite precursors with a smaller lateral size have a higher possibility of rapid oxidation due to the shorter diffusion length.⁶² Graphite oxide with abundant carbon–oxygen bonds can be promptly exfoliated with smaller lateral sizes. It is noteworthy that various factors, such as high oxidation temperature, long oxidation time and a high concentration of oxidizing agent, generally produce GO with a smaller lateral size, irrespective of the precursor graphite source. For instance, GO sheets with a lateral size of up to 220 and 10 μm could be obtained by a simple ultrasonication of GO with a C/O ratio of 2.63 and 2.08, respectively, in 5 min.⁶³ It has been reported that the oxidation of graphite takes place both through cross-planar and edge-center ways. The abundance of cross-planar oxidation in graphite oxide leads to the reduction of a lateral size of the resulting GO. Pan *et al.* suggested that large GO sheets (>100 μm) can only be taken from partially oxidized graphite particles through a mild mechanical shaking or ultrasonication for a short time.⁶⁴ Ultrasonication can result in the periodic cracking of GO sheets, while the inclusion of oxygen in the crystal lattice decreases the C–C bond energy. Once a crack is formed on an isolated GO sheet, it continuously grows with the external stimuli from sonication or mechanical shaking, while creating a build-up of tensile load in the sheets, finally resulting in smaller GO sheets.⁶⁴ Overall, all these factors, such as size and crystallinity of the graphite precursors, extent of oxidation, and duration of exfoliation (mechanical shaking/ultrasonication), are closely interconnected. Hence the variation of a single factor can largely influence the aspect ratio of GO sheets, which in turn can affect the LC behavior of GO, as will be discussed later in this section in detail.

3.2.2. Structure of GO. The chemical profile of GO is similar to that of its parent graphite oxide, comprising both aromatic and aliphatic carbon regions with oxygenated functional groups (Fig. 4a and b). There is often an ambiguity about the presence or absence of carboxylic groups in the atomic structure models for graphite oxide, because even in the well-accepted Lerf–Klinowski model, the authors excluded carboxyl groups in their revised structural model.⁵⁷ By contrast, in the GO structure, a significant amount of carboxyl groups at the edges can be expected due to the facile nature of GO to undergo amine/amide functionalization.^{66,67} Unlike graphite oxide, GO is a monolayer (or a few layers). Many spectroscopic techniques, such as X-ray photoelectron spectroscopy (XPS), Raman spectroscopy, Fourier transform infrared spectroscopy (FT-IR), and nuclear magnetic resonance spectroscopy (NMR), are commonly used for the identification and quantification of oxygenated carbons in GO.

In addition, scanning transmission electron microscopy (STEM) annular dark field (ADF) imaging combined with electron energy loss spectroscopy (EELS) is efficient for understanding the electronic structure of GO by measuring the carbon and oxygen K-edges and the low-loss electronic excitations in GO.⁶⁸ Erikson *et al.* validated the Lerf–Klinowski structural model of graphite oxide (Fig. 4a) established in 1998, albeit with modifications for monolayer GO with the help of high-resolution transmission electron microscopy (HR-TEM) in 2010.⁶⁹ They observed much larger graphitic (16%) and oxidized regions (82%) than proposed by the Lerf–Klinowski model. In addition, they also observed holes (2%) throughout the GO sheets. The holes were formed from the release of CO and CO₂ during the aggressive oxidation reaction (Fig. 5a–c). They observed that the oxidized regions form a continuous network across the carbon lattice, with no particular order between the primary and dominant (hydroxyls and epoxies) and edge (carbonyl) functionalities. Grossman *et al.* gave further evidence for GO structure with nanocrystalline regions of the sp² lattice. As suggested from the systematic direct imaging from suspended GO sheets and selected area electron diffraction (SAED) pattern, defective regions limit the size of the crystalline regions (Fig. 5d–g).⁷⁰

Along with the experimental observations, theoretical studies have also been extensively used to explore the puzzling atomic structure of GO. Density functional theory (DFT) calculations confirmed the experimental observations that the epoxide groups are in line with the carbon plane, while the hydroxyl groups are on the opposite side of the carbon plane, akin to the Lerf–Klinowski structural model for graphite oxide. Several studies also propose the band gap opening of GO.^{66,71,72}

3.2.3. Dispersibility of GO in aqueous/organic solvents. The dispersibility of GO in a solvent is strongly governed by the nature of the solvent and the surface functionalities in GO. According to the abundance of oxygen functional groups, GO can dissolve to form a stable dispersion in water and polar organic solvents, such as DMF, NMP, THF, and ethylene glycol, whereas nonpolar solvents generally show a low dispersibility of GO.^{8,61,73} Several groups reported that GO can be dispersed in chloroform, acetone, isopropanol, and DMSO up to 0.5 mg mL⁻¹, but with only a few hours of stability.⁷⁴ It is not the solvent

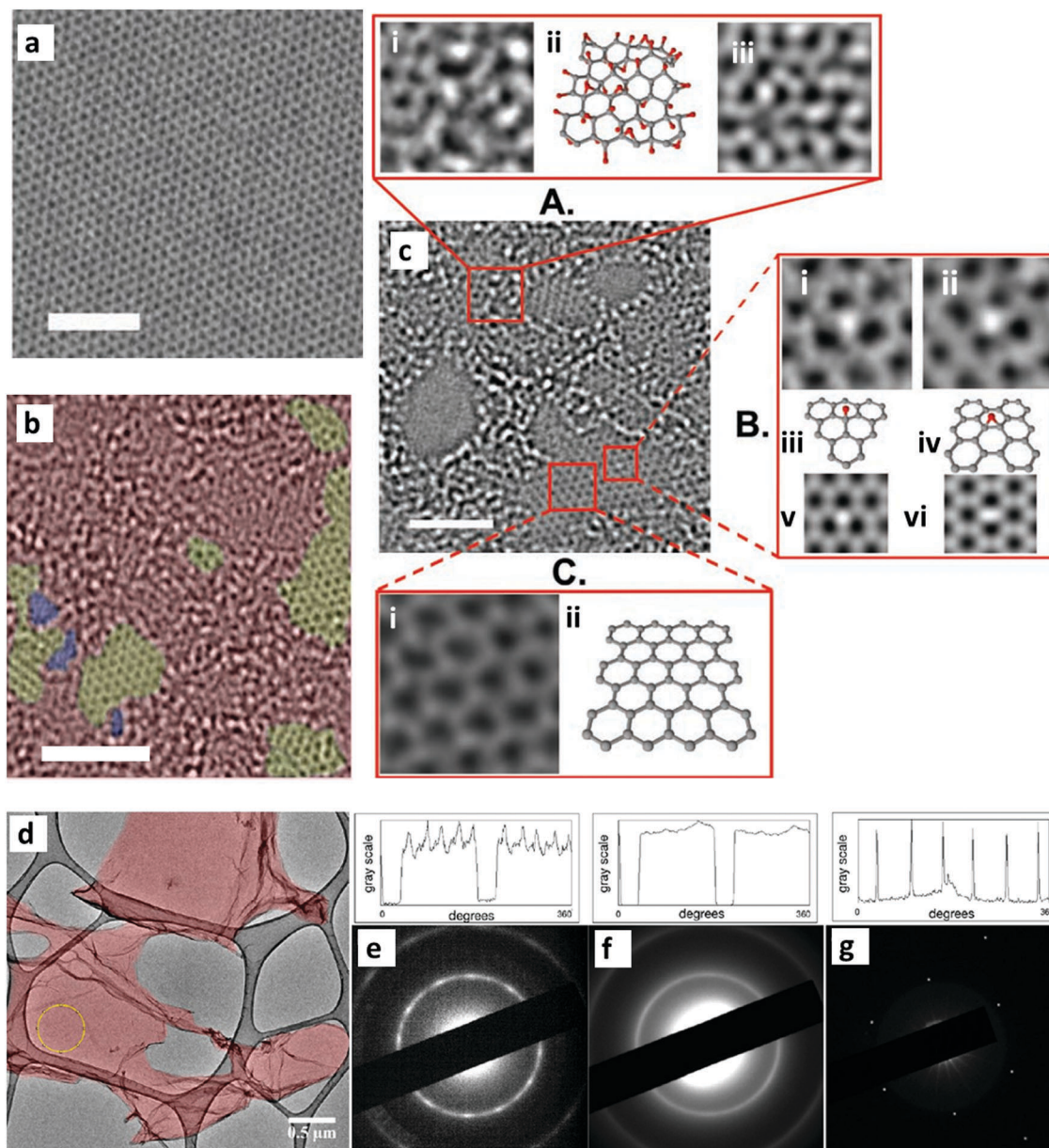


Fig. 5 TEM image of (a) pristine graphene displaying a perfect crystal lattice, (b) GO displaying the crystal lattice with defects. For better visibility, false colors were used to differentiate between regions of the disordered crystal lattice due to oxygen functionalities (red), graphitic areas (yellow), and holes (blue). (c) Three regions in the GO crystal lattice are enlarged, (A(i): highly oxidized, B(i and ii): focusing on the white spot in the graphitic region, C(i): graphitic). The TEM images in the B region display an isolated oxygen atom, probably at a hydroxyl position (Bi), and oxygen placed at an epoxy position (Bii). A probable atomic structure is proposed for the respective region in A(ii), B(iii and iv), and C(ii) in which carbon and oxygen atoms are represented with gray and red colors, respectively. A(iii) and B(v and vi) are the simulated TEM images corresponding to the atomic structural model A(ii) and B(ii and iv), respectively. In all images, the scale bar is 2 nm. Reproduced from ref. 69 with permission from John Wiley and Sons, copyright 2010. (d) TEM image of suspended monolayer GO sheets and (e and f) corresponding selected area electron diffraction patterns (SAED) displaying the nanocrystalline nature of GO (e) and the amorphous nature (f). SAED patterns in e and f correspond to the 200 nm region and yellow circled region in d, respectively. (g) SAED pattern for crystalline pristine graphene displaying sharp spots arranged in hexagonal pattern is given for comparison. Line scans associated with the SAED pattern are given in the top of respective SAED images, reproduced from ref. 70 with permission from the American Chemical Society, copyright 2016.

polarity that solely determines the long-term stability of the GO dispersion. For instance, GO forms a stable dispersion in NMP, but not in DMSO, despite these sharing the same net dipole moment (4.09 D) with NMP.⁶¹ Another major hypothesis is that the surface tension of the solvent and GO should be matched in order to have a minimum free energy of mixing for the long-term stability.⁸

The classical Derjaguin–Landau–Verwey–Overbeek (DLVO) theory has also been used to understand the GO dispersion and stability behavior.⁷⁵ According to DLVO theory, there are two principal repulsive forces among charged particles like GO: the surface charge originating from an electrical double layer (EDL) and the steric effect due to the bulky surface groups

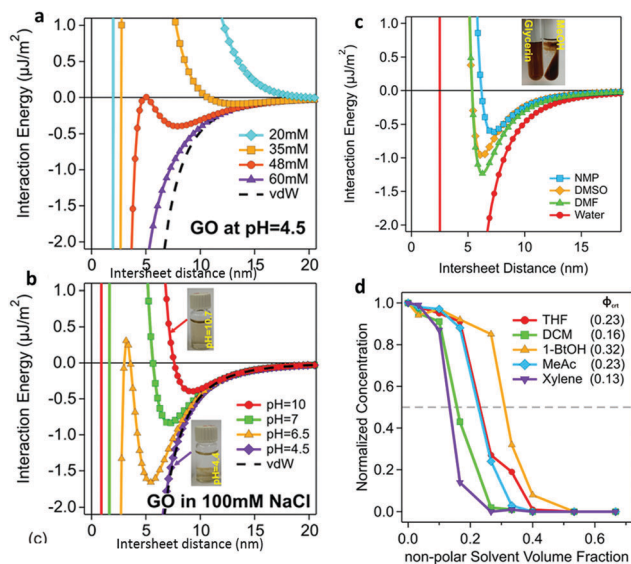


Fig. 6 Colloidal stability of GO in solvents explained by DLVO theory: DLVO interaction energy of two parallel GO sheets (a) at different ionic strength dispersions, but a fixed pH of 4.5 and (b) at different pH dispersions, but a fixed ionic strength (NaCl) of 100 mM concentration. The figure shows that at low pH and high ionic strength, van der Waals force dominate, leading to the aggregation of GO (inset in (b)). (c) DLVO interaction energy of two GO sheets in different solvents. Insets are photographs of a 1 mg mL^{-1} dispersion of GO in methanol and glycerine in the presence of 1 M HCl. The graph indicates that GO is stabilized by the solvent, which has a larger molecular size and a strong enough interaction with GO. The solvation force brings the unpredicted stabilization even at high ionic strength in organic solvents like NMP and DMF. (d) Normalized concentration of GO at different volume fractions of nonpolar solvents. The critical aggregation volume fraction (ϕ_{cr}) is given in the inset, which indicate that the solvents with high dielectric constant aggregate GO at lower volume fractions, reproduced from ref. 77 with permission from the American Chemical Society, copyright 2016.

repelling the imminent particles. DLVO theory attributes the synergy of these repulsive interactions for the colloidal stability. The pH is also important for the stability of the GO dispersion. In basic pH conditions, GO sheets are homogeneously dispersed in aqueous solution due to the repulsive interaction among GO sheets with deprotonated charged functionalities. By contrast, acidic pH conditions yield a visible aggregation of GO sheets, as the ionization of GO is weak in the low pH conditions, leading to insufficient electrostatic repulsion to avoid restacking.⁷⁶ In the same vein, a high ionic strength decreases the EDL distance due to a screening effect from the counter ions (Fig. 6).⁷⁷

Recently, molecular simulation studies have theoretically validated the thermodynamics and kinetic behaviors of GO sheets in a solvent media.^{78,79} These studies suggest that, for negatively charged GO sheets, the enhanced hydrogen bonding between deprotonated carboxyl groups and water molecules increases the colloidal stability. By contrast, in a nonpolar organic solvent, such as benzene, such a hydrogen bond-induced solvation is not available to overcome the attractive interaction among GO sheets, leading to aggregation. For neutral GO sheets, the electrostatic interaction among water molecules and GO sheet creates a net repulsive action between the GO sheets to help

dispersion. Interestingly, the hydroxyl groups seem to influence the dispersion stability of the neutral GO sheet more in an aqueous environment compared to carboxyl groups as the amount of carboxyl group is much lower than hydroxyl groups.^{79,80}

3.3. Liquid crystallinity of GO

Generally, anisotropic particles in a highly dilute dispersion exist in an isotropic phase. Upon the increase of particle concentration, a biphasic state gradually grows, where the isotropic and nematic phase co-exist, which finally stabilizes in a fully developed LC state. Similarly, GO can transit from a colloidal isotropic to nematic LC phase in water and some polar solvents. The mechanism of GOLC formation can be explained by the Onsager theory of excluded-volume effect formulated in 1949.⁸¹ In simple terms, the excluded volume of a particle can be understood as the volume that is unavailable for other particles due to the presence of a pre-existing particle. In a charged colloidal system, the charged particles exist at a certain distance from each other. According to Onsager theory, LC phase formation in colloidal systems is purely entropy driven and arises due to the competition between the low orientational entropy and the gain in the positional entropy. For instance, GO sheets are far apart and have a full degree of freedom for movement in a dilute dispersion. Hence, GO sheets have maximum orientational entropy in dilute concentrations (isotropic dispersions). By contrast, as the GO concentration increases, neighboring GO sheets come closer, leading to an overlap of the excluded volumes of neighboring GO sheets. Consequently, the degree of freedom of individual GO sheets is restricted, leading to a loss of orientational entropy. At this point, GO sheets tend to arrange in parallel (nematic ordering) to minimize the excluded volume and to maximize the packing entropy (positional/translational entropy). The loss of orientational entropy is compensated for by the increment in positional entropy, and the system becomes thermodynamically stable. At this transition concentration, typically known as the critical concentration, we can observe a clear phase separation of the isotropic and nematic phases. It is noteworthy that the structure of GO is more complex than the ideal rigid rod considered by Onsager's theory. The extent of orientational entropy loss in a rigid rod is not comparable to that of semi-flexible system like GO. While rigid particles lose orientational entropy as a whole, each segment of GO will lose configurational entropy by a different extent. Also, the electrostatic repulsion and steric hindrance among GO sheets were not considered in the theoretical framework.⁹

Phase transition from an isotropic to nematic phase in the GO dispersion can be adequately explained by Onsager theory even though refinements should be welcomed.⁹ For instance, we discovered such a LC phase transition in an immobilized GO aqueous dispersion at a concentration as low as 0.05 wt% (Fig. 7a).² However, the critical concentration for the isotropic to nematic phase transition varies for different GO samples due to the intrinsic polydispersity in the lateral size and shape of GO sheets (Fig. 7b and c). A clearer explanation for such a variation can be derived from Onsager theory, which states that the critical concentration for LC phase formation is directly

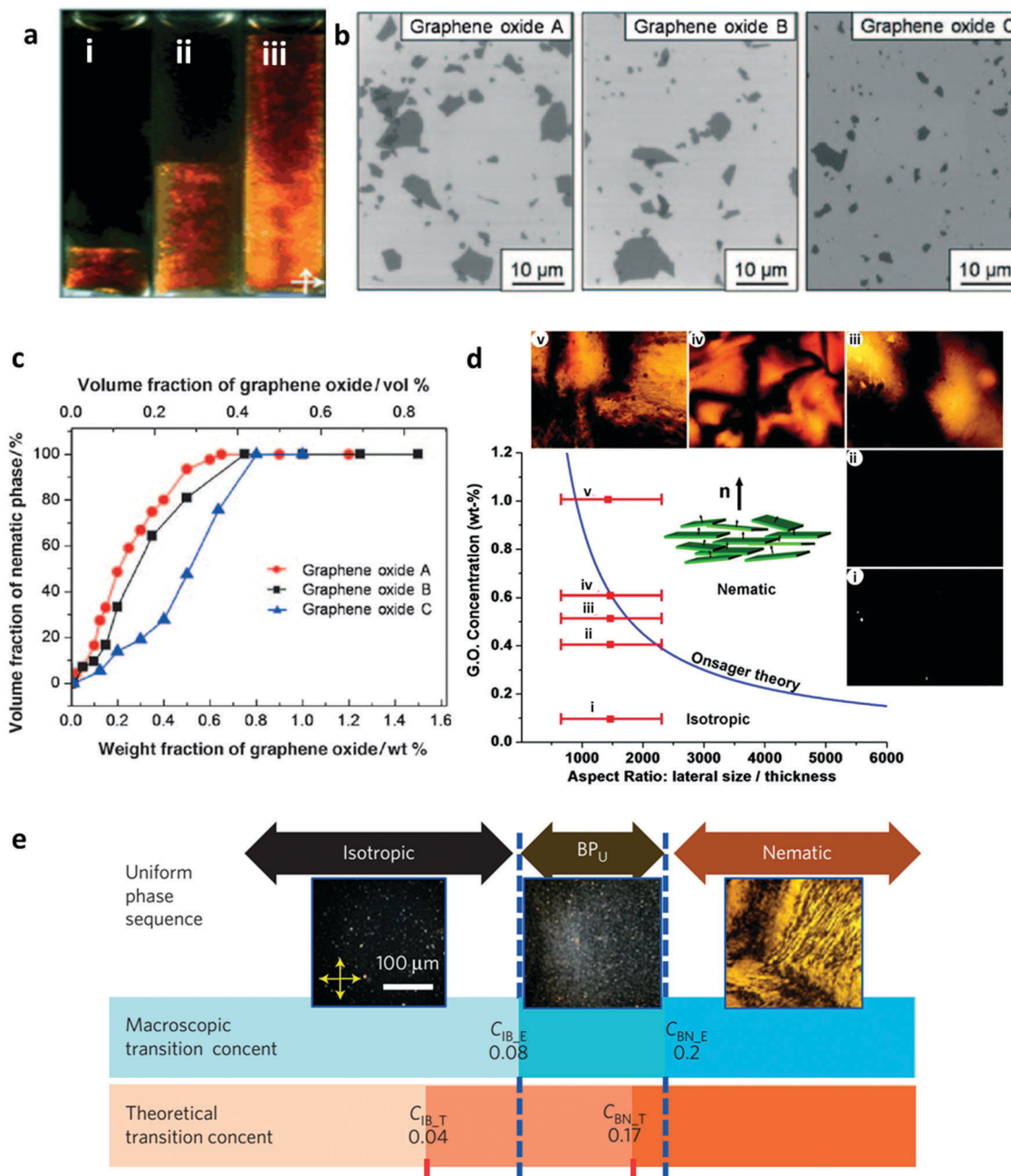


Fig. 7 LC behavior of GO: (a) optical images of GO dispersions of different concentration (i, ii, and iii represent 0.05, 0.2, and 0.5 wt%, respectively) under crossed polarizers showing bright birefringence associated to the nematic LC phase. (b) Scanning electron microscopy (SEM) images of GO sheets synthesized using different graphite sources. The aspect ratios (diameter/thickness) of the graphene oxide (GO) A, B, and C were 1600, 1200, and 700, respectively. (c) The change of nematic phase volume fraction with weight and volume fraction of graphene oxide A, B, and C. The graph clearly indicates that the higher the aspect ratio, the higher will be the nematic volume fraction at a constant weight/volume fraction; reproduced from ref. 2 with permission from John Wiley and Sons, copyright 2011, (d) GOLC phase diagram displaying the nematic to isotropic transition of GO dispersions of different aspect ratios in correlation with the Onsager model ($d/l \approx 5\rho GO)/(\rho \text{ suspension } C)$, where d : diameter, l : sheet thickness, ρ : density, and C : concentration at the phase transition; reproduced from ref. 7 with permission from the American Chemical Society, copyright 2011. (e) Experimental and theoretical comparison of concentration for sequential phase transition from isotropic, to biphasic (BP_U) and to the nematic phase with corresponding optical images under crossed polarizers. The acronyms CIB and CBN represent the concentration for transition from isotropic to biphasic and biphasic to nematic, respectively, and E and T represent the experimental result and theoretical value, respectively; reproduced from ref. 13 with permission from Springer Nature, copyright 2014.

proportional to four times the thickness and inversely proportional to the width of a particle. It is obvious that highly exfoliated GO sheets (preferably monolayer) with a large lateral dimension will

form the nematic phase at a much lower concentration than thicker and smaller GO sheets (Fig. 7d).⁷ For instance, Gao *et al.*, pointed out that the isotropic to nematic biphasic

transition occurred at a low concentration of ~ 0.03 wt% and the fully nematic phase was achieved at ~ 0.5 wt% for monolayer GO sheets with a thickness of ~ 0.8 nm, and lateral width of ~ 2.1 μm .⁶ In a separate report, Aboutalebi *et al.* reported that a fully developed nematic phase can be achieved in an extremely low concentration of 0.1 wt% with GO sheets of lateral area 10^3 μm^2 .³⁸ It is hard to match the theoretically predicted critical concentration values and experimental results (Fig. 7e), since not only the polydispersity of GO sheets, but also the electrostatic interaction among the surface functionalities of GO influence the excluded volume in a complicated way. Several other parameters, such as ionic impurities, salt concentration, and type of solvent, can also alter the critical concentration of GOLC formation and sometimes hinder the LC formation completely.

Generally, polydisperse plate systems are expected to show a discotic nematic phase only (Fig. 8a). However, Gao *et al.* reported that a highly concentrated GOLC (over 10 mg mL⁻¹) exhibited a higher order lamellar phase and helical LC ordering (Fig. 8b and c).⁶ Chiral LC ordering is generally expected from 1D colloidal particles, like DNA and viruses, and is non-traditional for achiral particles, like GO. The authors reported a gradual evolution from the nematic schlieren phase to the cholesteric phase and finally to a grandjean texture of the helical twist grain boundary phase typical of chiral LCs in polarized optical microscopy (POM) images along with the gradual increase of GO concentration in water. They proposed a twist-lamellar-block model, in which GO exists as blocks, which concurrently have both a lamellar and helical structure (Fig. 8d).

The authors attributed the repulsive interaction among negatively charged GO sheets for this unique phase behavior. It was later reported that polyacrylonitrile-grafted GO also exhibits such chiral lamellar LC behavior (Fig. 8e and f).⁸² The chiral LC behavior can be important in the spinning of GOLC into an aligned fiber form, which is widely popularized these days and will be discussed later.

As mentioned earlier, a phase separation between the nematic (high density) and isotropic (low density) phases can be achieved when a GO dispersion of low concentration is immobilized for a long period of time. However, such a process is generally very time consuming. Recently, another approach using dielectrophoresis was introduced, which can electrically accelerate the phase separation of isotropic–nematic, biphasic–nematic, or low-density–high-density nematic GOLCs.⁸³ A drawback with this method is that the phase separation cannot be sustained for a long time after the electric field is turned off. Nevertheless, this method makes it possible to attain an arbitrary-shaped phase separation and provides a versatile option for the manipulation of GO particles for specific material fabrication and device operation.

3.3.1. Principle and influencing factors for GOLC stability.

As introduced above, GOLC formation depends on many factors such as the concentration of GO, aspect ratio of GO sheets, including the lateral area and number of layers, and degree of polydispersity in the entire sample. There are also other critical factors that can adversely affect the stability of a GOLC.⁸⁴ For instance, ionic impurities are an inevitable addition in the as-prepared GO solution since the synthesis procedure of GO usually involves an acid treatment accompanied by salt dissolution.

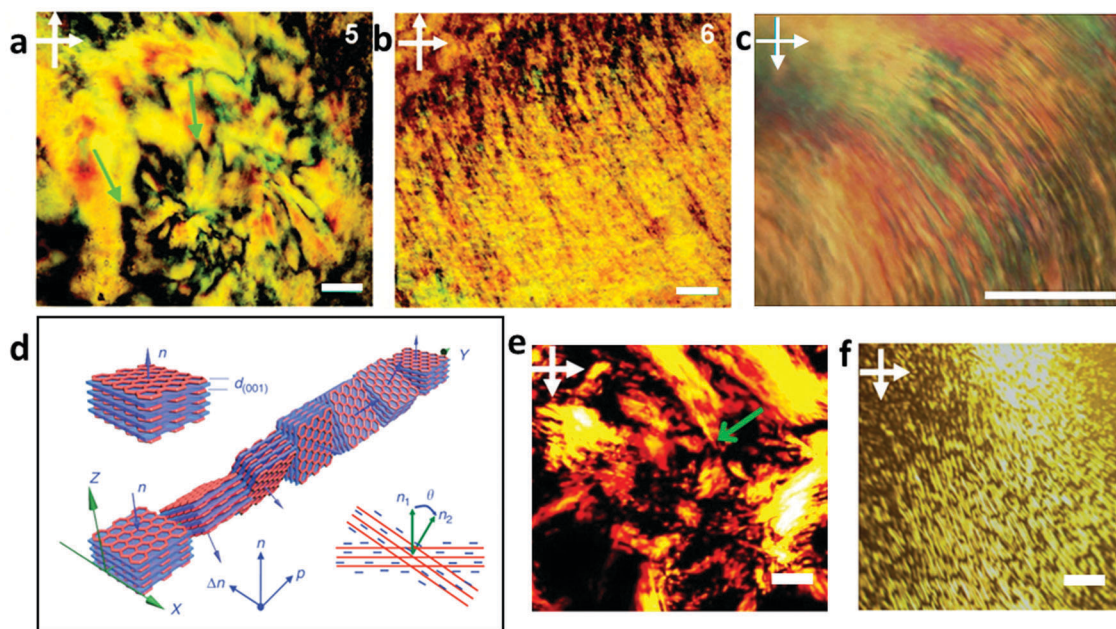


Fig. 8 Different LC phases of GO. POM images of (a) nematic (b) lamellar, and (c) chiral GOLC; scales in a, b, and c are 200, 200, and 300 μm , respectively. (d) Schematic of proposed twist-lamellar-block model for chiral GOLC. The red color denotes GO sheets and blue lines denote the negative charges, which repel two GO blocks with an angle resulting in a twisting (bottom right); reproduced from ref. 6 with permission from Nature Communications, copyright 2011 (<http://creativecommons.org/licenses/by/4.0/>). (e) Nematic LC phase and (f) lamellar LC phase of polyacrylonitrile grafted GOLC (scale: 200 μm). The volume fraction was 0.52% and 1.16%, in e and f, respectively; reproduced from ref. 82 with permission from the American Chemical Society, copyright 2013.

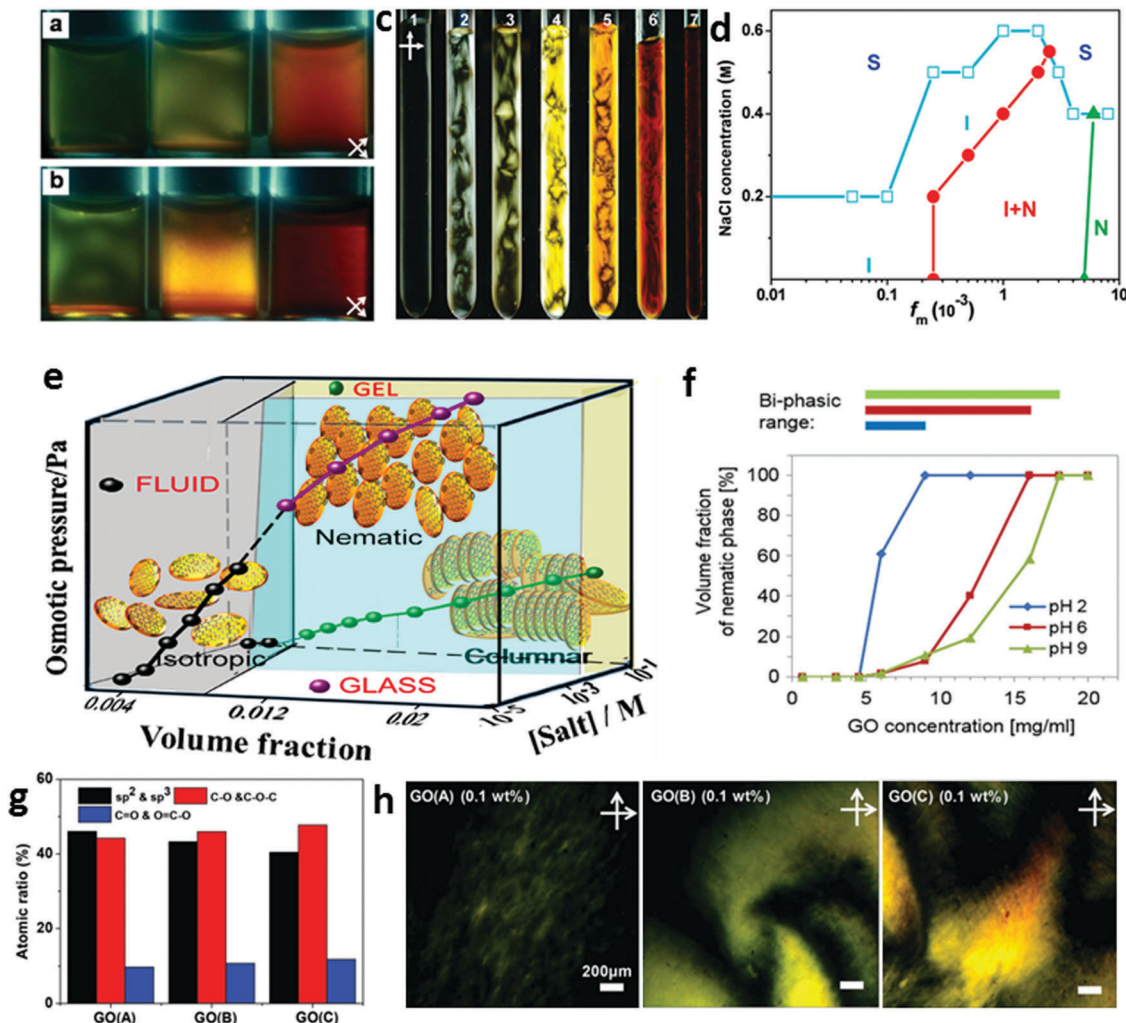


Fig. 9 Influencing factors for the formation and stability of GOLC (a and b) 0.1, 0.2, and 0.4 wt% (left to right) GO dispersion (a) without any dialysis treatment and (b) after dialysis treatment. Due to the presence of acidic and ionic impurities, the samples shown in (a), which are not dialyzed, showed only weak birefringence. Significant precipitation of GO can also be observed. The samples in (b), which are free of acidic and ionic impurities, show typical isotropic to nematic biphasic phase separation. Reproduced from ref. 2 with permission from John Wiley and Sons, copyright 2011. (c) POM images of GO dispersions of different mass fractions (f_m : 1.0×10^{-4} , 2.5×10^{-4} , 5×10^{-4} , 1.0×10^{-3} , 5×10^{-3} , 1.0×10^{-2} , and 2.0×10^{-2} from 1 to 7) without the presence of any salt. As shown, GO evolves into three phases: isotropic (I), biphasic coexistence (I + N), and nematic (N) when $f_m < 2.5 \times 10^{-4}$, 2.5×10^{-4} to 5×10^{-3} , and $> 5 \times 10^{-3}$, respectively. (d) Phase diagram of GO dispersion in water plotted with mass fraction of GO and the concentration of salt in the dispersion, indicating that at high salt concentration, the I + N phase diffuses into the I-phase and finally to the solid phase (S); reproduced from ref. 6 with permission from Nature Communications, copyright 2011 (<http://creativecommons.org/licenses/by/4.0/>). (e) Phase diagram showing a GO aqueous dispersion consisting of fluid, glass, and gel state simultaneously existing with LC order at a higher volume fraction and lower salt concentration; reproduced from ref. 10 with permission from the American Chemical Society, copyright 2014. (f) Influence of the solution pH on the extent of formation of the nematic phase for GO aqueous dispersions of different concentrations. As shown, the I + N biphasic region gets broadened at high pH 8.5. (g) Quantitative analysis of the degree of functionalization in three different GO samples and (h) corresponding POM images at a concentration of 0.1 wt%. As shown, the GO (C) with high oxygen functionality shows the brightest birefringence. Reproduced from ref. 182 with permission from John Wiley and Sons, copyright 2017.

During the discovery of GOLC, we found that the presence of excessive ionic impurities hinders the formation and/or the stability of the LC phase (Fig. 9a and b). It is therefore crucial to implement suitable purification procedures, such as membrane purification. Gao *et al.* investigated in detail salt-dependent LC formation from GO aqueous dispersions containing different NaCl concentrations (Fig. 9c and d).⁶ They reported a zeta potential value of -64 mV as ideal for GO dispersions to have a stable LC phase. Konkena and Vasudevan demonstrated the coexistence of

gelation and LC phase formation in a single framework with other arrested states, such as fluid and glassy states, for a GO aqueous dispersion.¹⁰ According to the authors, each of these states can be accessed by varying either the volume fraction and/or ionic strength of the medium. For instance, while at higher salt concentrations and volume fractions, the GO fluid state transforms to a gel form exhibiting nematic to columnar liquid crystal transition, glassy arrested states dominate at a low salt concentration (Fig. 9e). Similarly, the solution pH is also an

important factor for the stability of GOLCs in aqueous media (Fig. 9f).⁸⁵ When the pH of a GOLC decreases, the functional groups of GO become less protonated, resulting in a sudden decrease in the electrostatic repulsive interaction among GO sheets, consequently disrupting the LC phase and causing the coagulation of GO. Increasing the pH of the GO aqueous dispersion to higher basic regions (pH = 14) also results in the aggregation of GO sheets due to the partial reduction of GO by the high concentration of alkali.⁸⁶ Majumder *et al.* recently reported that polydispersity in both the sheet dimensions and surface charge density influence the isotropic to nematic phase transitions in GO dispersions.^{85,87} When the pH of a GO dispersion is greater than the pK_a of the carboxylic acid groups on GO, the polydispersity of the size and charge is enhanced, which leads to the phase separation of large GO sheets into the nematic phase and smaller GO sheets into the isotropic phase. Another important finding was that the amount of oxygen functionalities in GO determines the balance of the attractive and repulsive forces among the sheets. The higher the oxygen functionalities, the greater the fraction of the nematic phase (Fig. 9g and h). Notably, the zeta potential and solubility of GO in water also depend on the degree of oxidation, and hence, the oxidation method and the type of functionalities also influence the GOLC formation and eventual stability. Accordingly, a small change in any of these parameters, such as the mass/volume fraction, size/aspect ratio, degree of oxidation, pH, zeta potential and ionic strength, can have a critical influence on the GOLC stability. A recent report by Al-Zangana *et al.* appraised the importance of the surrounding geometric confinement in the GOLC formation and stability.¹⁸⁴ They reported that GO flakes confined between a parallel glass substrate tend to show homeotropic alignment and hence a pseudo-isotropic behavior due to the strong anchoring interaction of GO to the hydrophilic glass substrate. Nevertheless, either by increasing the GO flake size or by lifting the boundary conditions (increasing the gap between the parallel glass plates), enhanced LC phase formation could be achieved. When employing GOLCs in practical applications, all these above discussed factors should be taken into account.

Alternatively, the noncovalent modification of GOLC with amphiphilic polyelectrolytes consisting of a hydrophobic backbone and hydrophilic ionic groups, such as sodium poly(styrenesulfonate) and poly[2-(methacryloyloxy)ethyl]dimethyl-(3-sulfopropyl)-ammonium hydroxide, have been found to stabilize aqueous GOLCs. This is possible even in saturated NaCl and/or pH ranging from 1 to 13, which in turn extends the application of GOLCs in biological systems with an extremely high ionic strength environment.⁸⁸

3.3.2. Synthesis of GOLCs in an organic solvent. GOLCs in volatile organic solvents may facilitate the processability and widens their potential application fields, due to the compatibility of organic solvents with other materials, such as polymers and their feasibility for device fabrication. As discussed before, graphite oxide can directly exfoliate in organic solvents, such as *N*-methyl pyrrolidone (NMP), *N*-dimethylformamide (DMF), tetrahydrofuran (THF), and ethylene glycol, by ultrasonication.⁶¹ Severe ultrasonication can break the GO sheets into smaller fragments,

leading to a high critical concentration of LC phase formation, which can even eventually ruin the LC phase formation.⁷³ Alternatively, solvent exchange of an aqueous GOLC through a series of centrifugation–redispersions approach has been reported to achieve GOLCs in a wide range of organic solvents with long-term stability.⁸ The minimum GO concentration for isotropic to nematic phase transition was reported to be in the range of ~ 0.25 to ~ 0.5 mg mL⁻¹ for the tested polar organic solvents. The LC behaviors of GO in these organic solvents is comparable with that in aqueous media, as long as the polarity of the organic solvents enables extensive hydrogen bonding with the GO sheets. In addition, the intrinsic steric hindrance induced by the electrostatic repulsion between charged GO sheets should compensate for the unfavorable loss of rotational entropy associated with nematic ordering.⁸ Gudarzi *et al.* claimed that graphite oxide could directly exfoliate into GO in polar aprotic solvents, such as NMP and DMF, even in acidic media by simple hand shaking and could form a stable LC phase.⁷³ According to the authors, aprotic solvents offer similar nucleophilic interaction as that of water and induce a keto–enol transition in graphite oxide, resulting in the ionization of oxygen groups and consequently aiding in the swelling and exfoliation of graphite oxide to GO. In addition, the fact that polar aprotic solvents can hold a nucleophilic interaction even in acidic media, while the nucleophilicity of water decreases at a highly acidic environment, is an added advantage for GOLCs in aprotic polar solvents. From an application point of view, the polar aprotic solvents generally have high boiling points and are very difficult to remove completely. In order to achieve GOLCs in low boiling point polar organic solvents, such as alcohols, the preferable approach is the centrifugation–redispersion approach as mentioned before. Alternatively, organic functionalization of GO can be an effective strategy for obtaining an organic LC phase as reported by Poulin *et al.*,⁸⁹ who modified GO flakes with a PAPMS-*b*-PDMS copolymer, which exhibited a nematic LC phase in nonpolar organic solvents, such as diethyl ether, with a low boiling point. LC phases of GOs functionalized with polymers, such as polyacrylonitrile and poly(glycidyl methacrylate) in DMF have been also reported.^{82,90} Such a discovery of GOLCs in organic solvents has expanded the potential for the self-assembly process of GO with other inorganic and organic components, such as SWCNT or polymers, for forming aligned hybrid 3D structures of GO with desirable properties.

3.4. General characterization methods for GOLCs

As for most LC materials, GOLCs are also optically anisotropic with the refractive index depending on the polarization of light. Hence the optical birefringence test (either with the naked eye or under optical microscopy) is used as a typical tool for the identification of GOLCs, where the sample is placed between two crossed polarizers. GOLCs under crossed polarizers will be bright with contrasting domain areas, whereas GO sheets are oriented in different directions. For instance, in GO dispersions immobilized for a sufficiently long time, as shown in Fig. 7a, the upper dark portion represents the optically inactive isotropic phase, whereas the lower bright portion represents the birefringent

nematic region. As mentioned above, nematic, lamellar and chiral LC phases have been suggested for GOLCs so far. Nematic and chiral phases have signature textures when viewed under a polarized light source, and so X-ray measurements can be useful to distinguish between nematic and lamellar phases. Fig. 10a represents the typical schlieren texture for the nematic phase, revealing the local orientation of GO sheets with $\pm 1/2$ strength disclinations. Fig. 10b shows the detailed disclination

morphologies of a GOLC upon the successive rotations of crossed polarizers.³⁸ The disclination lines are densely formed among the nematic domains, which can gradually become annihilated by the mutual coupling of disclination lines with opposite strengths.⁹¹ More information from the analysis of the GOLC can also be obtained from the series of optical images for a GO dispersion with increasing concentration, as shown in Fig. 9c, where a clear transition from the isotropic to biphasic

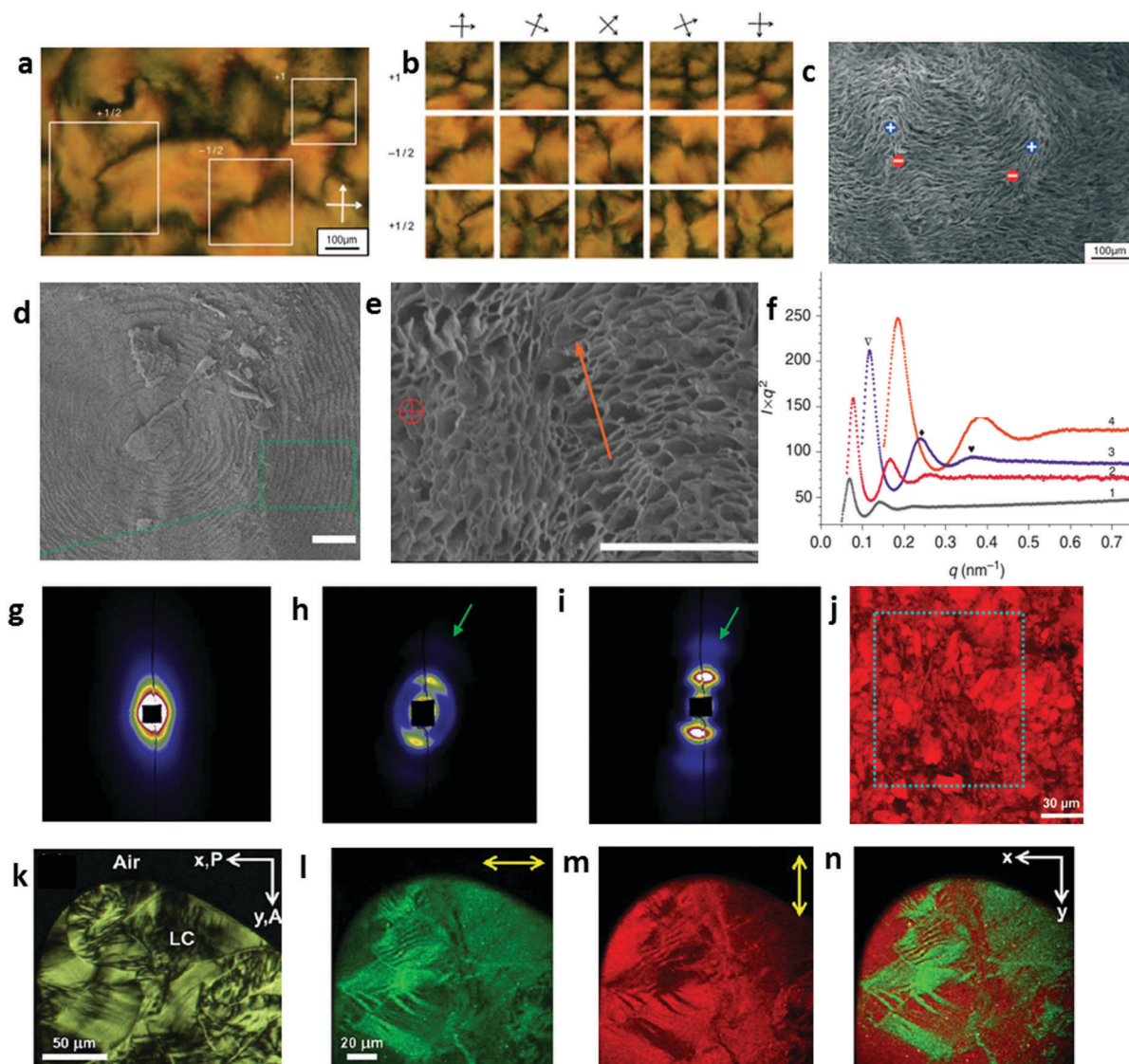


Fig. 10 Characterization methods for GOLC. (a) POM image showing a nematic schlieren texture of GOLC with different disclinations ($+1/2$, $-1/2$, and $+1$). (b) Change in the disclination morphology upon sequential rotations of crossed polarizers conveyed by the rotation of brushes in different directions. (c) SEM image of nematic GOLC freeze-dried sample. Blue and red color marks in the image represent the direction of $+1/2$ and $-1/2$ disclinations, respectively; reproduced from ref. 2 with permission from John Wiley and Sons, copyright 2011 (d) SEM image of GO chiral LCs confined in a circular cavity. (e) Magnified top region in (d) displaying the dislocation of neighboring GO lamellar blocks with twist vectors. (f–i) SAXS analysis of a GO dispersion with different volume fractions (ϕ_s). (f) Scattering intensity profiles of GO dispersions of ϕ_s 0.38%, 0.91%, 1.5%, and 2.12% numbered 1, 2, 3, and 4, respectively, indicating the lamellar ordering of GOLC. (g–i) 2D scattering patterns of GO dispersions of ϕ_s (g) 0.38%, (h) 0.91%, and (i) 1.5%. The diffusive arcs highlighted by arrows indicate reflection arcs. (j) Confocal laser microscopy image of nematic GOLC displaying an orientational alignment of GO sheets into vertical and parallel focal planes; reproduced from ref. 6 with permission from Nature Communications, copyright 2011 (<http://creativecommons.org/licenses/by/4.0/>). (k) POM image of 1.2 wt% of GOLC confined between untreated glass substrates under crossed polarizers. (l and m) Nonlinear photoluminescence images of GOLC for different polarizations as directed by the arrows and (n) overlaid PL images displayed in l and m; reproduced from ref. 92 with permission from the American Chemical Society, copyright 2012.

and finally to a full nematic phase is revealed.⁶ The GO dispersion in tube 1 is fully isotropic, and hence optically inactive. The birefringence with thread-like textures represents the evolving biphasic (tube 2) and the colorful fully covered birefringence represents the nematic phase (tube 6). A uniform brightness birefringent image is possible only if a well-aligned director scale is present and can be related to a fully developed single LC phase.

Along with the optical birefringence test, the scanning electron microscopy (SEM) imaging of a freeze-dried GOLC can also provide a straightforward visualization of the LC phase. For instance, half disclination (+1/2 and -1/2) cores can be easily identified from the SEM image of a nematic GOLC (Fig. 10c). Annual ring-like structures made of undulating bands with discrete boundaries are shown in the SEM image of a chiral GOLC (Fig. 10d and e). It is noteworthy that low-temperature freezing or a sample fracture step may induce artifacts in the sample morphology, so careful sample preparation is crucial for reliable characterization. Additionally, SAXS (small-angle X-ray scattering) is a superior tool to characterize the presence of long-range order. SAXS diffusive pattern along with SAXS profiles plotted with X-ray scattering intensity (I) as a function of the scattering vector modulus ($q = 4\pi \sin \theta / \lambda = 2\pi/d$) have been used to analyze the structure of GOLCs. Strong anisotropic diffusive patterns and multiple scattering peaks were indexed to the (001) reflections signature of a higher order lamellar structure in GOLCs, proposing a lamellar nature (Fig. 10f–i). Besides, under visible light, GO flakes are highly fluorescent and thus the orientational order in GOLCs can be identified by confocal laser microscopy or non-linear photoluminescence imaging (Fig. 10j–n).^{6,92}

3.5. Physical properties of GOLCs

3.5.1. Rheological properties. The rheological properties (also known as flow properties) of a material depend on both the structural arrangement of constituent particles and the interactive forces among the particles.⁹³ Understanding the rheological properties is important for LC systems, because a thorough knowledge of the rheology of LCs should facilitate their processing.²⁷ The rheological properties of GOLCs have been reported several times.^{5,94,95} Generally, the viscosity behavior of a GO dispersion depends not only on the GO composition but also on the molecular arrangement. It has been confirmed that during the isotropic–nematic phase transition, the shear viscosity of GO dispersion decreases significantly due to the LC alignment of GO sheets. Gao *et al.* reported a very low viscosity of 1×10^{-2} Pa s at a shear rate of 10 s^{-1} for a GO aqueous dispersion with a maximum mass fraction of 5×10^{-3} , which in turn implies that the GO alignment can be readily influenced even by weak external forces.⁵ In order to gain more insights into the shear thinning behavior of GOLCs, our group systematically investigated and modeled the variation of viscosity of GO dispersions at different GO concentrations.⁹⁶ As shown in Fig. 11a, the viscosity of a GO aqueous dispersion increases with the increase in GO concentration in the isotropic phase and reaches a maximum point at the onset of isotropic–nematic phase transition and

then decreases in the biphasic. The reduction of viscosity above the critical volume fraction ($\phi \sim 0.33$) can be attributed to the nematic LC ordering of GO sheets. In other words, the viscosity minima correspond to the GO concentration for the completion of isotropic–nematic phase transition. Not only the structural arrangement, but also the interparticle interactions have been found to influence the rheological properties of GO dispersion. For instance, Konkena and Vasudevan studied the effect of ionic strength on the viscosity of a GO dispersion at different concentrations.¹⁰ They concluded that in the presence of salt ions, the viscosity of the GO dispersion increases with concentration. The viscosity increase was relatively small even for a high-concentration GO dispersion at a low salt concentration. In contrast, at a high salt concentration, the viscosity increases rapidly with concentration. The presence of a large amount of salt ions in a GO dispersion reduces the Debye screening length and consequently screens the surface charges, which in turn enhances the surface attractive force, leading to increased viscosity.

Wallace *et al.* also contributed to the understanding of the rheological properties of GOLCs and demonstrated that the rheological properties can be controlled by adjusting the concentration of GO (Fig. 11b and c).⁹⁷ They further investigated the size effect of GO on the viscosity at a fixed GO concentration (2.5 mg mL^{-1}).⁹ Large GO sheets ($>1.5 \mu\text{m}$) show a fully nematic non-Newtonian behavior with yield values typical of shear thinning fluids; while intermediate-sized GO resulted in biphasic regions with a weak yield value, and small GO sheets ($<0.7 \mu\text{m}$) displayed the typical Newtonian behavior without any yield. Interestingly, the LC phase could be induced in isotropic GO dispersions with small sheets by mixing an equal volume of isotropic GO dispersions with large GO sheets (Fig. 11d and e). They also investigated the rheology of GO sheets with the same aspect ratio of 45 000 with different concentrations and found that the critical concentration of phase transition was much lower ($\phi \sim 2.2 \times 10^{-4}$) than the theoretically predicted value for a colloidal dispersion ($\phi \sim 0.5$). The authors measured the ratio of the elastic and storage moduli of GO dispersions for a range of frequencies (0.01–100 Hz), and differentiated four distinct regimes, namely viscoelastic liquid, liquid-to-solid transition phase, soft solid and a gel phase, in GO dispersions of increasing concentration. Recently Poulin *et al.* reported that a shearing of the GO dispersion decreases the spacing between GO sheets, and consequently, the fraction of aligned particles increases.⁹⁸ According to the authors, GO layers showed thermal undulations with a large amplitude under low shear, which, however, were then literally ironed out due to the genuine flexibility and large aspect ratio of the GO sheets (Fig. 11f and g). The bending rigidity of GO was reported to be 1 kT, which is almost 2 order of magnitude lower than pristine graphene sheets, implying that the disruption of the graphene sp^2 crystal lattice by oxidation makes the GO sheet ‘super’ flexible. From an application point of view, the rheological properties of GOLCs play a significant role in their processing and in the determination of their structures and properties. For instance, the viscoelastic characteristics of

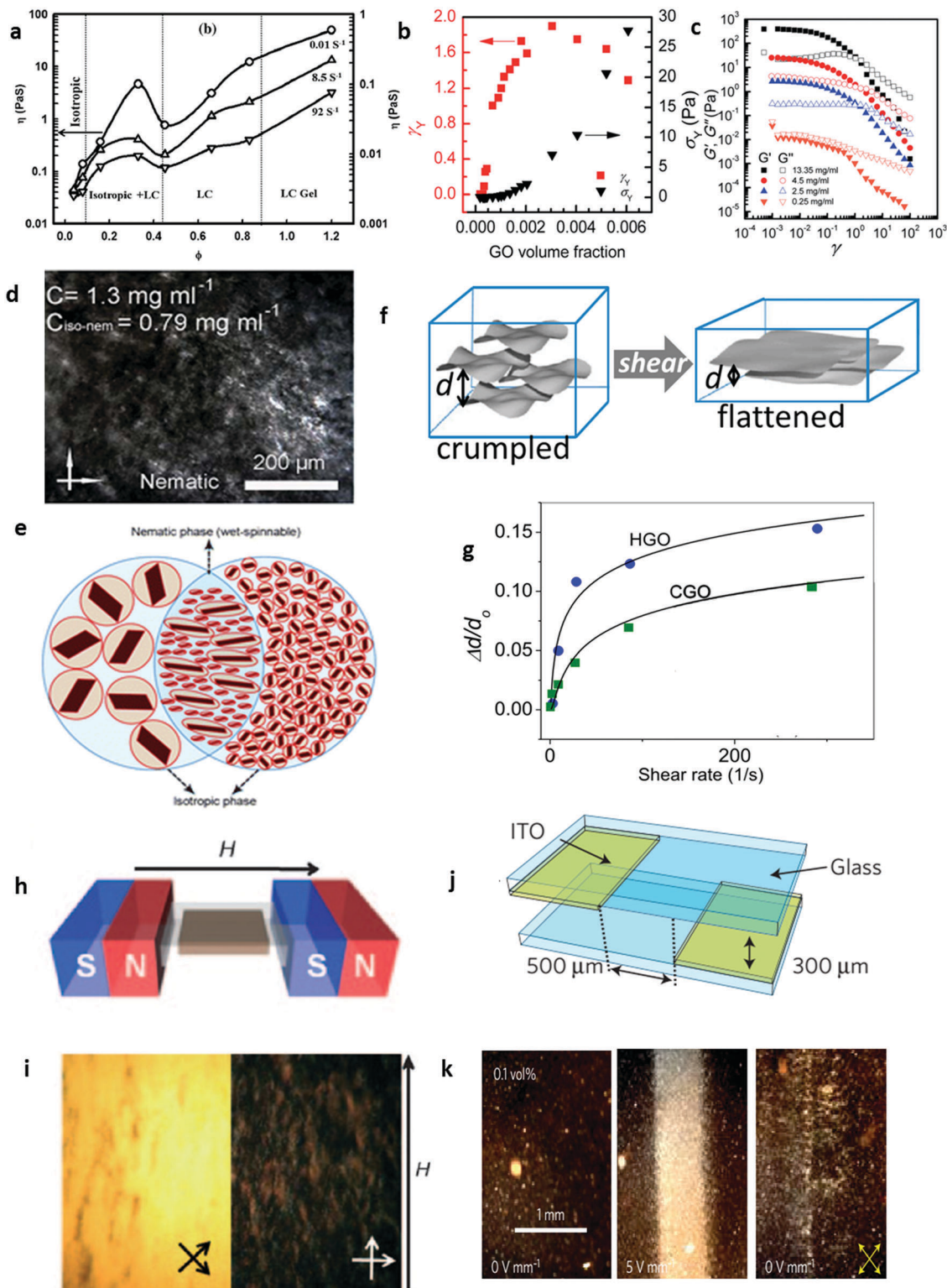


Fig. 11 Properties of GOLC. (a) Change of shear viscosity with the volume fraction of a GO aqueous dispersion and the corresponding phase diagram of isotropic to nematic phase transition; reproduced from ref. 96 with permission from Elsevier, copyright 2014. (b) Yield strain (γ_Y) and yield stress (σ_Y) of GO aqueous dispersions at varying volume fractions. (c) Variation of the storage (elastic) and loss (viscous) moduli of a GO dispersion at 0.01 Hz frequency under different strains; reproduced from ref. 97 with permission from the Royal Society of Chemistry. (d) POM image and (e) schematic of a nematic GOLC obtained by the mixing of two fully isotropic GO dispersions of ultralarge GO sheets and small GO sheets; reproduced from ref. 9 with permission from the Royal Society of Chemistry. (f) Schematic of shear-induced flattening of the GO flakes. (g) Normalized variation of the spacing between GO layers for two GO samples (HGO: homemade GO and CGO: commercial GO) as a function of the shear rate; reproduced from ref. 98 with permission from the National Academy of Science, copyright 2016. Experimental set up and corresponding POM images of (h and i) magnetic field- and (j and k) electric field-induced aligned GOLC. (h and i) Reproduced from ref. 2 with permission from John Wiley and Sons, copyright 2011, (j and k) reproduced from ref. 13 with permission from Springer Nature, copyright 2014.

GOLCs is very important in the wet-spinning of GOLC fibers, which is a noticeably growing application of GOLCs, as will be discussed in more detail later.

3.5.2. Magnetic and electro-optic properties. Upon the first discovery of GOLCs, we noted that the LC phase can be aligned by applying an external stimulus, such as a magnetic field (Fig. 11h and i).³⁸ Due to the weak intrinsic magnetism of GO sheets, nonetheless, it took several hours to complete the alignment. The alignment could be accelerated when GO sheets are functionalized by magnetic nanoparticles (Fe_2O_3). We also tested whether electric-field-induced alignment is possible, but found that due to the electrophoretic migration of charged GO sheets, they tend to be electrochemically reduced at cathodes under a direct current (DC) field. A practical solution to this problem was demonstrated by Song *et al.*, who employed a high-frequency (10 kHz) alternating-current (AC) field to prevent the electrophoretic migration (Fig. 11j and k),^{12,13} and found that a GOLC could be successfully aligned under an AC electric field with a high Kerr coefficient (1.8×10^{-5}), an indication of its high sensitivity to the electric field. The relaxation of such an E-field alignment was very short after the electric field was switched off. The birefringence gradually disappeared and GO sheets in the nematic phase diffused away. They further studied the influence of GO concentration and sheet size on its electro-optical properties, and concluded that a sheet size of $5 \mu\text{m}$ and concentration of 2 wt% gave optimum birefringence in the fastest response time, thus proposing the potential application of GOLCs as a new type of liquid crystal display (LCD).

3.6. Graphene-based liquid crystals other than GOLCs

3.6.1. Graphene LC (GLC). A pristine graphene liquid crystal (GLC) was reported by Pasquali *et al.* Following their previous discovery of LC phase of protonated SWCNT in a superacid dispersion, the authors found a similar behavior with graphene.⁴⁰ They reported the spontaneous exfoliation of graphite in chlorosulfonic acid, without any mechanical shaking/ultrasonication. The superacid protonated the graphite edges, which found their way into the interlayers and eventually destroyed the interlayer interaction in the graphite, resulting in the spontaneous dissolving of single layers of protonated graphene. A superacid dispersion of graphene at a concentration of 2 mg mL^{-1} was obtained by this spontaneous exfoliation. Redispersion of this protonated graphene at a concentration as high as 20 to 30 mg mL^{-1} exhibited birefringent schlieren texture, representing a colloidal nematic LC behavior (Fig. 12a). The same group reported a similar LC phase for a graphene oxide nanoribbon (GONR) and chemically reduced GONR (rGONR) in the superacid dispersion as well.^{40,82} A graphene thin film processed from a GLC was reported to show a remarkable electrical conductivity of $1000 \Omega \text{ cm}^{-2}$ and transparency of 80%. Although the discovery of GLC opened the possibility for the direct processing of pristine graphene, the superacid conditions for the GLC formation remain critical challenges for practical applications.

3.6.2. Graphite oxide LC (GtOLC). Both GO and also its parent graphite oxide (GtO) can display lyophilic nematic LC behavior at a high concentration in aqueous media, as reported by Tong *et al.*⁴² The authors reported that an aqueous GtO with a lateral dimension up to 31.3 nm and thickness up to 62.8 nm

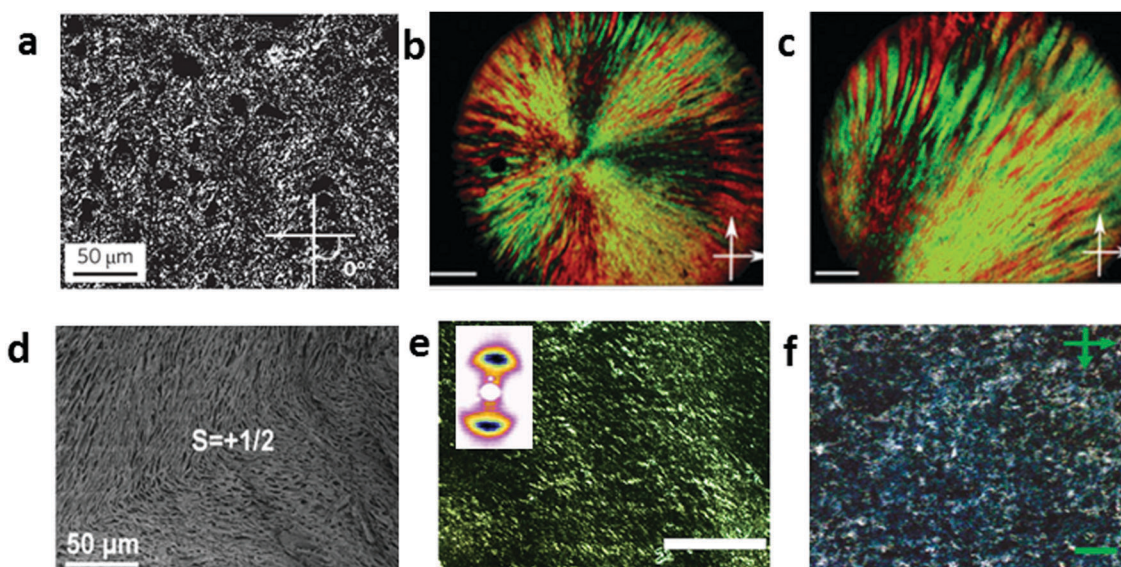


Fig. 12 Graphene-based LCs other than GOLC: POM image of (a) GLC in chlorosulfonic acid (2 wt%); reproduced from ref. 40 with permission from Springer Nature, copyright 2010. (b and c) GtLC in water (1.45 wt%) under crossed polarizers. (c) Magnified wave-like texture from the image given in (b). Scale bars are 200 and 100 nm in b and c, respectively. (d) SEM image of a freeze-dried GtLC (1.45 wt%) sample with a disclination (S) of $+1/2$; reproduced from ref. 42 with permission from the Royal Society of Chemistry. (e) POM image of bile-salt-functionalized rGO in water (5.9 wt%) under crossed polarizers (scale bar: 400 nm), with the corresponding SAXS 2D pattern given in the inset displaying butterfly-like patterns resulting from the nematic ordering. Reproduced from ref. 41 with permission from the American Chemical Society, copyright 2012. (f) POM image of hyperbranched-polyglycerol-functionalized rGO in DMF (3 mg mL^{-1}) between crossed polarizers (scale bar: 100 μm); reproduced from ref. 99 with permission from Scientific Reports, copyright 2012 (<http://creativecommons.org/licenses/by/4.0/>).

at a concentration above 1.45 wt% could display a typical thread-like schlieren texture of a nematic LC phase in a fan-like pattern, as observed under POM (Fig. 12b and c). Such a vivid wave pattern with a fan-like texture is commonly related to a lamellar or hexagonal columnar LC phase with a high anisotropy, which in turn suggests a coherent long-range ordering in the GtO. Further confirmation of the lamellar ordering in GtOLC was drawn from the SEM image of freeze-dried GtOLC, where an ordered self-assembly with a wave-like texture was clearly visible (Fig. 12d). Here, the optical textures of GtOLC sharply change from a green to a yellow-colored pattern with an external electrical field, representing an electric-field-induced alignment behavior, similar to GOLC.

3.6.3. Reduced graphene oxide LC (rGOLC). Due to the structural defects and oxygen functional group formation in the crystal lattice, GO is electrically insulating, unlike its counterpart pristine graphene and parent graphite. In order to restore the electrical conductivity, GO should be reduced to remove the oxygenated functionalities using chemical/thermal reduction methods to form reduced graphene oxide (rGO). Unfortunately, while the electrical conductivity can be restored, rGO loses its dispersibility in water/polar solvents and its LC phase behavior. Poulin *et al.* reported a practical solution to this problem by the functionalization of rGO with bile salt (Fig. 12e).⁴¹ Bile salt prevents aggregation and stabilizes rGO sheets in water and thereby tackles the most common problems associated with rGO, such as the restacking. The bile-salt-functionalized rGO was reported to show isotropic to nematic LC phase transition in the concentration range from 1.0 to 1.5 wt% in water. Alternatively, Gao *et al.* reported the nematic LC behavior of partially reduced rGO in DMF at a concentration of 3 mg mL⁻¹ (Fig. 12f).⁹⁹ The authors functionalized GO with hyperbranched polyglycerol followed by a low temperature reduction to achieve a high dispersibility in organic solvents. The reduction of GO in the presence of polymers is a critical challenge because of the possibility of the thermal/chemical degradation of polymers.

4. GOLC-based functional materials and applications

4.1. New concept of GOLC-based graphene functional materials

Graphene and GO have been intensively exploited to realize innovative materials that can surpass the limitations of conventional organic and inorganic materials. While pristine graphene has been widely considered for future electronics due to its unprecedented charge carrier mobility,¹⁰⁰ chemically active GO has established its own application fields, such as high-performance functional composites and energy storage/conversion based on the advantage of easy functionalization, hybridization and good processability.^{101–104} Despite the significant progress in GO-based materials, LC systems of GO have been seriously overlooked for developing a new class of GO-based materials. In the early days of research on GO, the principal applications were expected to be the solution casting or vacuum filtering of graphene films, papers, and sponges.^{105–108} In fact, anisotropic-layered interior structures of the diverse

forms of GO films did not attract much scientific interest. Nowadays, it is recognized that casting or vacuum filtering from a GO dispersion could be involved with the LC behavior, particularly upon evaporation or drainage of the solvent. The LC phase can lead to the enhanced alignment of GO sheets in those assembled structures, offering improved mechanical and electrical/thermal properties, compared to the random-oriented configuration of GOs. GOLCs have great potential to further broaden the range of applications for graphene or to enhance the properties of conventional graphene-based materials, based on the genuine spontaneous structural alignment of LCs.

4.2. Wet-spun GOLC-based fiber

Research attention on fiber-shaped graphene materials is ever increasing due to their potential to greatly expand the application spectrum of graphene. A fiber structure is highly desirable to exploit the appealing properties of graphene for wearable and flexible applications in electronics, biomedical monitoring and sensing and so on. However, the realization of graphene-based fiber has been retarded due to the lack of appropriate rheological properties or sheet interlocking methods for graphene or GO. The first fiber-shaped GO-based material was demonstrated upon the discovery of GOLC by our group.² GOLC enabled hand-drawn GO/poly(acrylic acid) nanocomposite fibers to be fabricated exhibiting clear birefringent schlieren textures with cross polarizers (Fig. 13a). GOLC fiber have an anisotropic alignment of GO sheets in the inner structure originating from pre-ordered LC domains in the colloidal GOLC dispersion, as shown in Fig. 13b. This seminal demonstration of GO fibers exploiting the high alignment of LCs suggested a new potential of LC-based graphene materials and triggered intensive research efforts in relevant works. GOLCs offer a unique combination of moderate fluidity, outstanding long-range ordering and strong inter-sheet interactions. These exceptional features enable suitable wet-spinning from a GO dispersion for making 1D fiber-shaped graphene-based materials.⁶ The formation of a graphene fiber *via* wet-spinning generally comprises sequential stages, including: (1) extrusion of GO dispersion through a fine nozzle, (2) solidification of the as-spun GO fiber in a coagulation bath, (3) rinsing, drying and (4) collecting (Fig. 13c).⁶ For a continuous wet-spun graphene fiber from a colloidal GO dispersion, suitable rheological properties as well as an efficient solidification mechanism are highly required.^{9,109} A GOLC dispersion can have a suitable rheological condition for the wet-spinning process, satisfying the requirement for a ratio of storage modulus to loss modulus ratio (G'/G'') of greater than 1, which is similar to the case for typical viscoelastic soft solids or gels. Interestingly, the rheological properties of GOLCs are readily tunable by the concentration and size of GO sheets.^{9,96} As the size of GO increases, the minimum GO concentration for suitable wet-spinning decreases. Adversely, a small-sized GO dispersion must be highly concentrated to form fibers *via* a wet-spinning approach. Due to the large distribution of GO sizes and shapes in a typical colloidal GO dispersion, the optimized concentration for wet-spinning process should be experimentally determined. The as-spun GO fiber must be solidified to maintain the robust 1D fiber structure commonly obtained by immersion

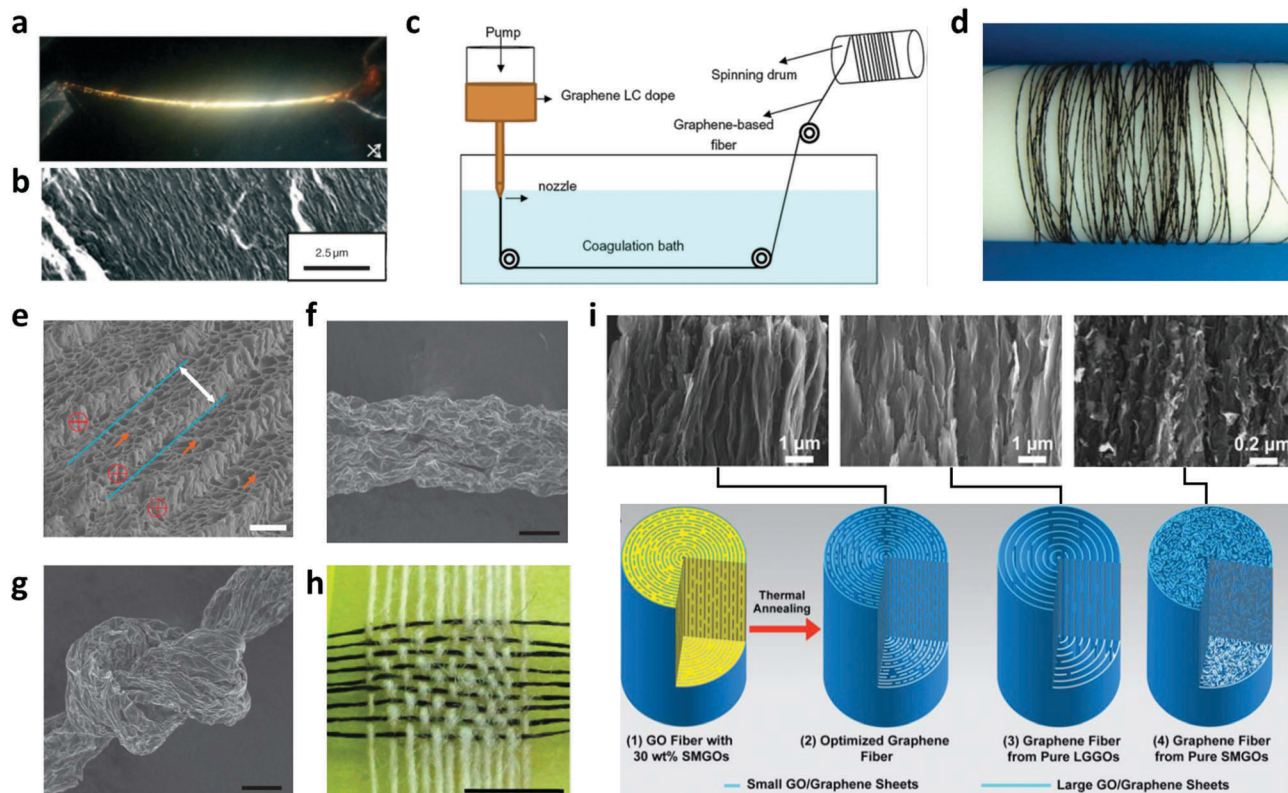


Fig. 13 Graphene fibers produced by a wet-spinning process with a colloidal GOLC dispersion. (a) Hand-drawn GO/PAA composite fiber. Clear birefringence indicates homogeneously dispersed, uniaxially oriented GO flakes. (b) Highly aligned GO morphology along the fiber axis. Reproduced from ref. 2 with permission from John Wiley and Sons, copyright 2011. (c) The schematic illustration for typical wet-spinning from GO liquid crystals to fibers; reproduced from ref. 183 with permission from Elsevier, copyright 2015. (d) Meter-long GO fiber wound on a Teflon drum of 2 cm diameter. (e and f) SEM images of the cross-section and surface of wet-spun graphene fiber. (g and h) Knot and woven structure made with the wet-spun graphene fiber. Reproduced from ref. 6 with permission from Nature Communications, copyright 2011. (i) Schematic illustration of the synthesis of SMGO-intercalated graphene fibers: (1 and 2) optimized graphene fiber with a highly ordered and compact structure with 30 wt% SMGOs filling into the microvoids; (3) graphene fiber spun from pure LGGOs showing a highly aligned inner morphology but loosely packed structure by microvoids; and (4) graphene fiber spun from pure SMGO dispersion showing a random alignment of GO flakes; reproduced from ref. 110 with permission from the American Association for the Advancement of Science, copyright 2015.

in a coagulation bath with appropriate chemicals/solvents.⁸² Some possible solidification mechanisms reported thus far are listed as below:

- (i) chelation using divalent cations, such as CaCl_2 and CuSO_4 , in water or in water/alcohol media;^{15,109–111}
- (ii) precipitation using non-solvents, such as acetone¹¹² and ethyl acetate;¹¹³
- (iii) dispersion destabilization using acid (H_2SO_4) and base (NaOH , KOH) in water or ethanol.^{6,109,114}

The coagulation stage is one of the most significant steps and exerts a significant influence on the inner structure and chemical composition of the final wet-spun fibers. In general, a fast coagulation rate leads to a rough surface and irregular cross-sectional shape with a porous morphology. In contrast, a sufficiently slow coagulation results in a relatively regular cross-section and compact inner structure.¹¹⁵ These morphological characteristics, in principle, influence the electrical/thermal conductivity and mechanical modulus of deoxidized graphene fibers. Graphene fiber with a high volumetric density possessing a closely packed interior generally exhibit an excellent electrical/thermal conductivity and mechanical modulus, arising from the

large mutual contact area among the inner sheets, compared to porous fiber.¹¹⁰ The chemical composition of solidified GO fiber is highly dependent on the composition of the used bath. In the case of coagulation by metal ion chelation, most chelated metal ions remain and exhibit their own physicochemical properties in the final graphene fibers.¹⁶

The first additive-free wet-spun GO fiber from a GOLC dispersion was reported by Gao *et al.*⁶ The GOLC dispersion was directly injected from a glass syringe into a coagulation bath of 5 wt% NaOH /methanol solution. The suitably concentrated GOLC dispersion (typical volume fraction = 5.7%) enabled a successful wet-spinning into continuous meter-scaled and flexible GO fibers with adjustable diameters of 50–100 μm (Fig. 13d). Highly aligned GO sheets were observed in the core part of the fiber in contrast to the rough surface morphologies (Fig. 13e and f). The as-spun fiber showed a Young's modulus of 5.4 GPa, tensile strength of 102 MPa and elongation at break of 6.8–10.1%. After conversion into the rGO fiber by chemical reduction using hydroiodic acid (HI), the electrical conductivity reached 250 S cm^{-1} . These fibers had sufficient mechanical flexibility and toughness to form knots and loosely woven patterns (Fig. 13g and h). After this

pioneering work, further advances have been achieved toward high-performance fibers.

The report on multifunctional graphene fiber by Lian *et al.* provided a remarkable advance in GOLC research.¹¹⁰ They demonstrated excellent electrically and thermally conductive and mechanically strong graphene fibers by inserting small-sized GO (SMGO) sheets into GOLC fibers, wet-spun from a large-sized GO (LGGO) LC dispersion (Fig. 13i). It is well recognized that large-sized GO sheets are necessary for high-performance GO-based materials, while reducing the number of physical junctions where mechanical failure or electrical contact resistance could easily occur.¹¹⁶ In this work, the graphene fiber even made of LGGO should have numerous micro-voids, causing a deterioration in the electrical, thermal and mechanical properties. However, such undesired micro-spaces were effectively filled by SMGOs, while maintaining the LC alignment of the LGGO backbone structure. After thermal reduction at 2850 °C, the LGGO fiber incorporated with 30 wt% SMGOs showed an outstanding thermal conductivity of 1290 W m⁻¹ K⁻¹, electrical conductivity of 2210 S cm⁻¹, Young's modulus of 135 GPa and tensile strength of 1080 MPa. Recently, Eom *et al.* showed the effect of multivalent cation binders, such as Co²⁺, Al³⁺, and Fe³⁺, on the fiber spinning of a GOLC solution. They showed trivalent ion coagulants were more effective for strengthening and stiffening the GO fiber than divalent ions for mechanical performance.¹¹⁷

According to accumulated knowledge from many reports on the wet-spinning of GOLC dispersions, the property enhancing or engineering of graphene fibers principally relies on the following key factors.

(i) Degree of GO alignment in the graphene fibers: this is the most fundamental factor for the overall properties, including the electrical, thermal, and mechanical properties. The degree of GO alignment is strongly dependent on the quality of the original GOLC dispersion and the shear field generated at the fiber extrusion nozzle.

(ii) Inter-sheet interaction within the graphene fiber: the aligned GO sheets in graphene fibers should have sufficient interactions with each other for the desired properties. This can be mainly controlled in the solidification stage by adapting a proper coagulation mechanism depending on the target applications. Here, the widely used metal ion chelation principle exploits strong ionic cross-linking between multivalent metal ions and abundant oxygen functional groups at the GO surface.

(iii) Defect control in the graphene fibers: for a high electrical/thermal conductivity and superior mechanical strength of graphene fibers, a densely packed inner structure without voids or defects is crucially required. In contrast, for energy storage applications, a porous inner structure can be beneficial for its large surface area as well as for the easy access of electrolyte ions. The defect density can be controlled by adjusting the composition of the GOLC dispersion, the coagulation rate, the drying condition, reduction method, and so on.

4.3. Paper, films, inks and foam based on GOLCs

Graphene-based materials have been commonly exploited in the form of papers, thin films and 3D porous foam structures

for many diverse applications. In particular, the 2D geometry of graphene-based materials has been intensively studied for innovative electronics, including transistors or transparent electrodes, or high-performance energy storage devices.^{100,118} Colloidal GO dispersions are commonly employed for the solution processing of those materials.⁴⁶ In contrast, despite their great potential, GOLCs have not been actively utilized for such purposes thus far. In this section, the advantages of GOLCs will be discussed in the processing of graphene-based materials with a focus on the property enhancement by LC alignment.

The vacuum filtration of an aqueous GO dispersion has been commonly employed for free-standing GO papers.⁴⁶ The directional flow of a GO dispersion through a membrane induces a layer-by-layer assembly of GO sheets with submicron-scaled wrinkles and waviness. This unique morphology is distinct from most paper-like materials and makes this material more resilient than traditional carbon- and clay-based papers. Li *et al.* reported a chemically converted graphene (CCG) dispersion and fabricated free-standing films using vacuum filtration.¹¹⁹ As-prepared CCG films exhibited an excellent electrical conductivity (72 S cm⁻¹) and mechanical property (Young's modulus = 35 GPa). GOLCs have turned out to be advantageous for highly aligned GO sheets in a GO paper or film (Fig. 14a and b). The improved packing density and ordering results in the enhanced electrical and mechanical properties of the graphene-based structures.

The vacuum filtration and drop-casting of colloidal GO dispersions has inherent limitations in the scaling-up and continuous production, which are significant considerations for practical manufacturing. Similar to the fiber-shaped graphene materials discussed above, a continuous GO film has been successfully fabricated by a wet-spinning technique from a GOLC dispersion (Fig. 14c).¹²⁰ GO films of 20 m length and 5 cm width were continuously fabricated at a rate of 1 m min⁻¹ (Fig. 14d). The film thickness was dependent on the spinneret width ranging from 1.5 to 10 μm. Owing to the pre-ordered LC domain in the GOLC dispersion, the wet-spun GO film demonstrated a highly aligned and densely packed inner structure, thereby showing sufficient mechanical property for strolling or weaving for clothes-integrated applications (Fig. 14e).

Printing techniques are promising approaches for the direct drawing of desired patterns in devices or materials. A suitable ink formulation is one of the key components for a reliable and sophisticated printing technique. To the end, the proper rheological properties of ink are essential to form a stable droplet and to impinge on a target substrate. To meet the demanded viscoelasticity of printable inks, a graphene-based ink with 20% ethylene glycol in NMP has been used for the printing of thin film transistors (mobility of 95 cm² V⁻¹ s⁻¹) and transparent electrodes (transmittance of ~80% and sheet resistance of ~30 kΩ □⁻¹) (Fig. 14f and g).¹²¹ Beyond 2D or planar printing, recently, there has been rapid progress in graphene 3D printing for 3D free-standing piles, rings or any other macroscopic shapes. It is noteworthy that most of the available graphene-based ink formulations contain organic additives to facilitate suitable rheological properties, which can seriously deteriorate the intrinsic fascinating properties of graphene in the drawn patterns.

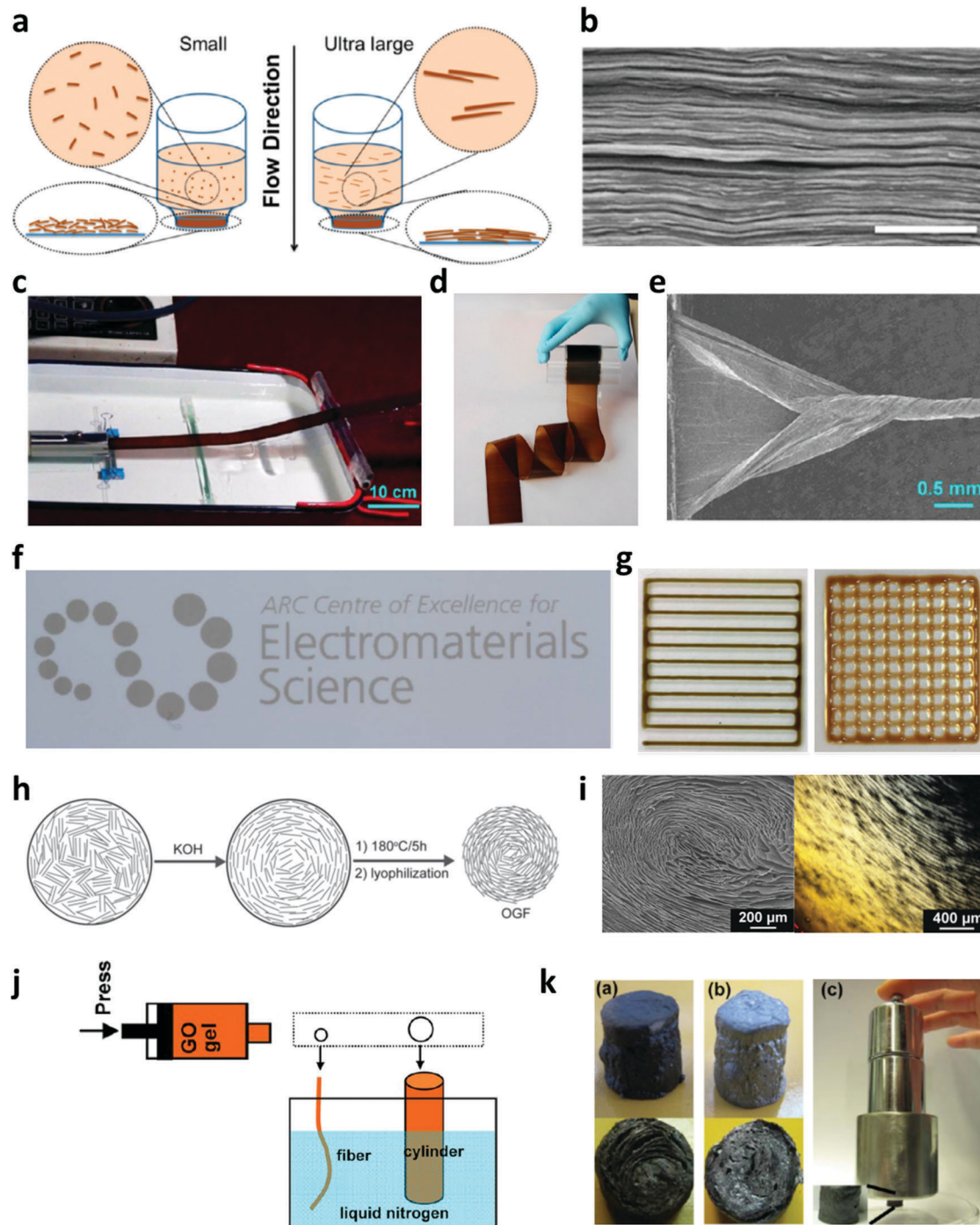


Fig. 14 Various form of GOLC-based materials. (a) Schematic illustration of self-assembly through the vacuum filtration of small- and large-sized GO dispersion. (b) SEM images cross-sectional area of GO papers; reproduced from ref. 116 with permission from the American Chemical Society, copyright 2012. (c) Photograph of the wet-spinning of a continuous GO film through a geometrically confined spinning channel. (d) Wet-spun GO film wound on a glass reel. (e) Wet-spun GO film being scrolled to a fiber shape reproduced from ref. 120 with permission from the American Chemical Society, copyright 2014 (<https://pubs.acs.org/doi/full/10.1021/cm5033089>). (f) Ink-jet printing with a GOLC viscoelastic dispersion. (g) Extrusion printed pattern (left) and 3D architecture (right) with a GOLC viscoelastic dispersions of 4.5 mg mL^{-1} and 13.3 mg mL^{-1} , respectively; reproduced from ref. 121 with permission from the Royal Society of Chemistry. (h) schematic illustration of the fabrication of ordered graphene foam. (i) SEM images of a graphene aerogel with highly aligned graphene sheets and POM images of a GO suspension. Reproduced from ref. 14 with permission from John Wiley and Sons, copyright 2016. (j) schematic illustration of the preparation of porous GO fibers and cylinders. (k) Photographs of a GO porous cylinder and the section plane after cutting (left), photographs of reduced graphene porous cylinder and the section plane (middle), and photograph of a 42 mg GO porous cylinder lifting 900 g poise (right); reproduced from ref. 124 with permission from the American Chemical Society, copyright 2012.

A GOLC system approach allows fine tunability in rheological properties of GO by adjusting the concentration and the flake size of GO without any other additives. This can be a valuable route to the reliable pure graphene printing of complicated patterns demanded for innovative graphene devices.

Based on the well-developed gelation techniques from a colloidal GO dispersion,^{122,123} GOLC can be directly adapted to conventional gelation principles and can yield superior material properties by improving the inter-sheet interaction arising from enhanced GO sheets ordering. For example, graphene aerogels with long-range ordered microstructures were prepared from a GOLC dispersion through a conventional hydrothermal process and subsequent freeze-drying.¹⁴ Highly oriented GOLC was induced at a low concentration by increasing its pH with potassium hydroxide (KOH) (Fig. 14h). The ordered graphene foam had a high conductivity (0.42 S cm^{-1}), low density (13.2 mg cm^{-3}) and good elasticity (repeated compression to 60% over 500 cycles) (Fig. 14i). Also, the suitable rheological properties of GOLC could be exploited for the preparation of 3D graphene cylinders. By adjusting the size of the spinning nozzle, three-dimensional porous GO cylinders (diameter of 1 cm) with aligned pores were produced by the wet-spinning of GOLC gels (Fig. 14j).¹²⁴ After chemical reduction with HI, the porous rGO cylinder exhibited a compression modulus of 3.3 MPa with a density as low as 71 mg cm^{-3} . This compression modulus value is an order of magnitude higher than rGO aerogels comprised of randomly oriented GO sheets (390 kPa) (Fig. 14k).

4.4. Flake size selection for functional graphene-based materials

As mentioned above, the GO sheet size is a decisive parameter for the electrical and mechanical properties of final graphene-based materials. Those material properties are definitely determined by the density of the junction among GO flakes and the supernumerary edge defects in the material, at which electrical contact resistance or mechanical failure occurs. Supernumerary edge defects deteriorate the interface property at the junctions by disturbing the strong surface-to-surface interaction between GO flakes. Large GO flakes (typically $>20 \mu\text{m}$) effectively minimize these disadvantages of conventional GO-based materials compared to typical small GO flakes. The sonochemical exfoliation of GO from graphite typically yields a broad size and shape distribution. Huang's group demonstrated the spontaneous size separation of GO flakes based on the size-dependent amphiphilicity of GO sheets using a Langmuir–Blodgett (LB) assembly (Fig. 15a).¹²⁵ Energetically, large GO sheets having more hydrophobic basal planes prefer to be adsorbed at the air–water interface, while small GO sheets with abundant hydrophilic edges sink into the sub phase. Recently, our group proposed another principle for the spontaneous and additive-free selection of large-sized GO (LGO) based on a size-dependent LC phase transition (Fig. 15b).¹¹ A GO aqueous dispersion was prepared by a modified Hummer's method with mild stirring and sufficient dialysis to avoid mechanical damage generating undesired small pieces. Moderately concentrated GO dispersions enabled us to develop a biphasic LC structure having an isotropic phase of low density and a nematic phase

of high density. In the stabilized biphasic GOLC suspension, large-sized GO ($>20 \mu\text{m}$ of lateral size) were concentrated at the bottom precipitated nematic phase with a high density, while the low-density isotropic phase was composed of small-sized GO. Careful fractionation of the nematic phase GOLC at the bottom side allowed effective size selection of the LGO dispersion with minimizing the portion of small GO flakes. The effectiveness of LGO for enhancing GO-based material properties has been demonstrated in a wide range of research fields. The GO flake size also influences the doping behavior of graphene materials. In the N-doping process, LGO flakes allowed predominant quaternary N-doping type due to the large surface-to-edge ratio, while small GO flakes principally generated pyridinic N at the abundant edge sites (Fig. 15c).¹¹ Quaternary N is a more efficient catalytic site for the oxygen reduction reaction (ORR) than pyridinic N. As expected, the N-doped rLGO electrocatalyst shows a higher catalytic property than N-doped typical rGO flakes. LGO is also effective in the development of high-performance graphene-based composites. Our group developed composite materials consisting of highly aligned LGO structures in a polydimethyl siloxane (PDMS) matrix (Fig. 15d).¹²⁶ A nematic phasic LC LGO dispersion induced by geometrical confinement was freeze-dried to become a highly aligned GO aerogel. The resultant aerogel was infiltrated with PDMS and chemically converted into rGO by hydrazine. This kind of aligned structure of GO can effectively improve the performance of GO-based composites, compared to the randomly dispersed GO structure.

4.5. Electrodes for electrochemical applications: supercapacitors, secondary batteries and electrocatalysis

Supercapacitors and secondary batteries have attracted a great deal of research interests as powering devices to operate future portable/wearable electronics as well as electric vehicles. Fiber-shaped materials are quite advantageous for these purposes since their 1D geometry allows woven structures as well as a certain flexibility. In this regard, wet-spun graphene-based fibers produced from GOLC dispersions have been recognized as promising candidates for future wearable power sources, particularly due to their large specific surface area, high electrical conductivity and scalability from a continuous process.

While densely packed GO fibers are generally desired for strong inter-sheet interactions and an enhancement of the electrical and mechanical properties, fiber electrodes for high-power density must have a loosely packed open porous structure for the facile movement of electrolyte ions and a maximal surface area for storage.^{110,115,127} To this end, the porosity of graphene fiber has been increased by adjusting the coagulation rate during the graphene fiber formation process. The resultant loosely packed graphene fiber supercapacitors exhibited an excellent specific surface area of $2210 \text{ m}^2 \text{ g}^{-1}$ and outstanding charge storage capacitance of 409 F g^{-1} at 1 A g^{-1} .¹¹⁵ Another strategy to enhance the energy density of graphene fiber supercapacitors is the incorporation of pseudo-capacitive materials, such as metal oxides. Manganese dioxide (MnO_2), a well-known pseudo-capacitive material with several oxidation states, was incorporated into graphene fibers. Based on the synergistic

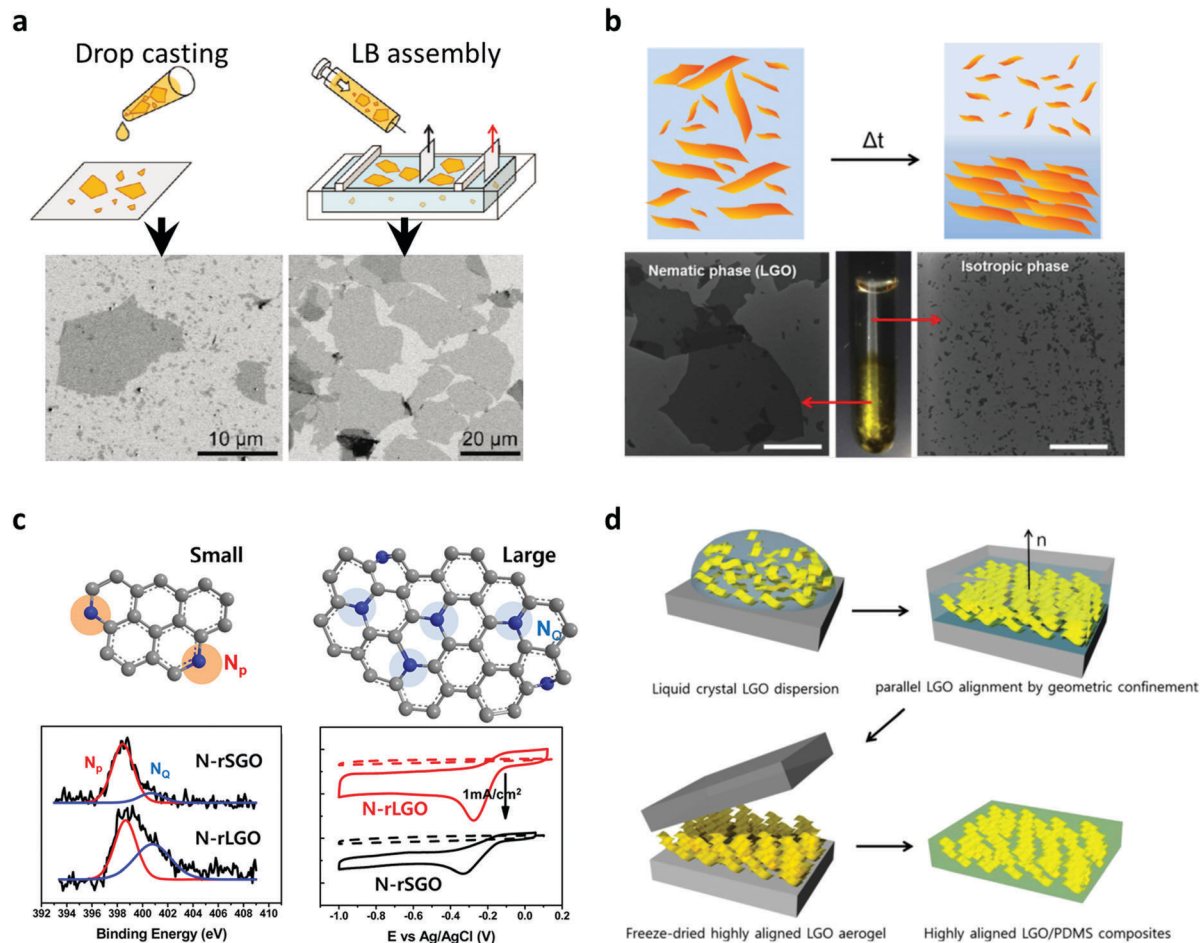


Fig. 15 Principles for large GO selection and LGO-based functional materials. (a) Spontaneous size separation during LB assembly using the size-dependent amphiphilicity of GO; reproduced from ref. 125 with permission from the American Chemical Society, copyright 2010. (b) Self-size separation by the spontaneous phase separation of a GOLC dispersion. (c) Schematic illustration of pyridinic N-dominant small GO and quaternary N-dominant LGO (top). N1s XPS deconvoluted peaks for N-doped reduced small GO and ORR electrocatalytic performance, reproduced from ref. 11 with permission from the American Chemical Society, copyright 2014. (d) Schematic illustration of the fabrication of LC-aligned LGO/PDMS composites; reproduced from ref. 126 with permission from Elsevier, copyright 2015.

energy storage mechanism of the redox reaction of MnO_2 and electrical double layer formation at the surface of graphene, the graphene/ MnO_2 fiber electrode materials showed a high areal capacitance of 59.2 mF cm^{-2} , *i.e.*, five times higher than that of pristine graphene fibers.¹²⁸

In general, a large specific surface area and suitable electrical conductivity are essential requirements for high-performance energy storage electrodes. In graphene fibers, unfortunately, the relationship between the porosity and electrical conductivity of graphene fiber is inversely proportional, while the abundant pores in the loosely packed graphene fiber restrict the electrical pathway per unit cross-sectional area. Our group have suggested one possible way to address the challenge is by introducing a highly crystalline conducting polymer thin layer, which could play the role of an additional electrical pathway, as well as pseudo-capacitive materials (Fig. 16a).¹⁶ Interface confirmed polymerization at a heteroatom-doped graphene fiber surface enables the high crystalline growth of a semiconducting polymer (PEDOT, polyaniline, polypyrrole) thin layer tightly bonded to the

graphene surface. The incorporation of conducting polymer layers significantly enhanced the electrical conductivity of graphene fibers from 148.6 to 387.1 S cm^{-1} . Owing to the active pseudo-capacitive behavior of the conducting polymer layers, the PEDOT/graphene fiber exhibited excellent volumetric capacitance of 417.9 F cm^{-3} , compared to the neat graphene fibers of 29.1 cm^{-3} . In addition, we found that the macropores in the graphene fiber act as an electrolyte reservoir, which channel the electrolyte in the entire electrode volume. Wearable and rechargeable fiber-shaped batteries have been recently demonstrated by the wet-spinning of an active materials/GOLC mixture dispersion. Geng *et al.* reported linear fiber-shaped lithium-ion batteries (LIBs) based on wet-spun titania (TiO_6)/GO fibers (Fig. 16b).¹²⁹ The 2D titania nanosheets were properly assembled into macroscopic GO fibers, regularly stacked and conformally hybridized *in situ* with rGO. The novel composite fiber electrodes offered excellent mechanical properties as well as outstanding electrochemical performance in terms of linear densities (0.19 mg cm^{-1}), rate capabilities (89 mA h g^{-1} at 0.0425 mA) and cyclic behaviors

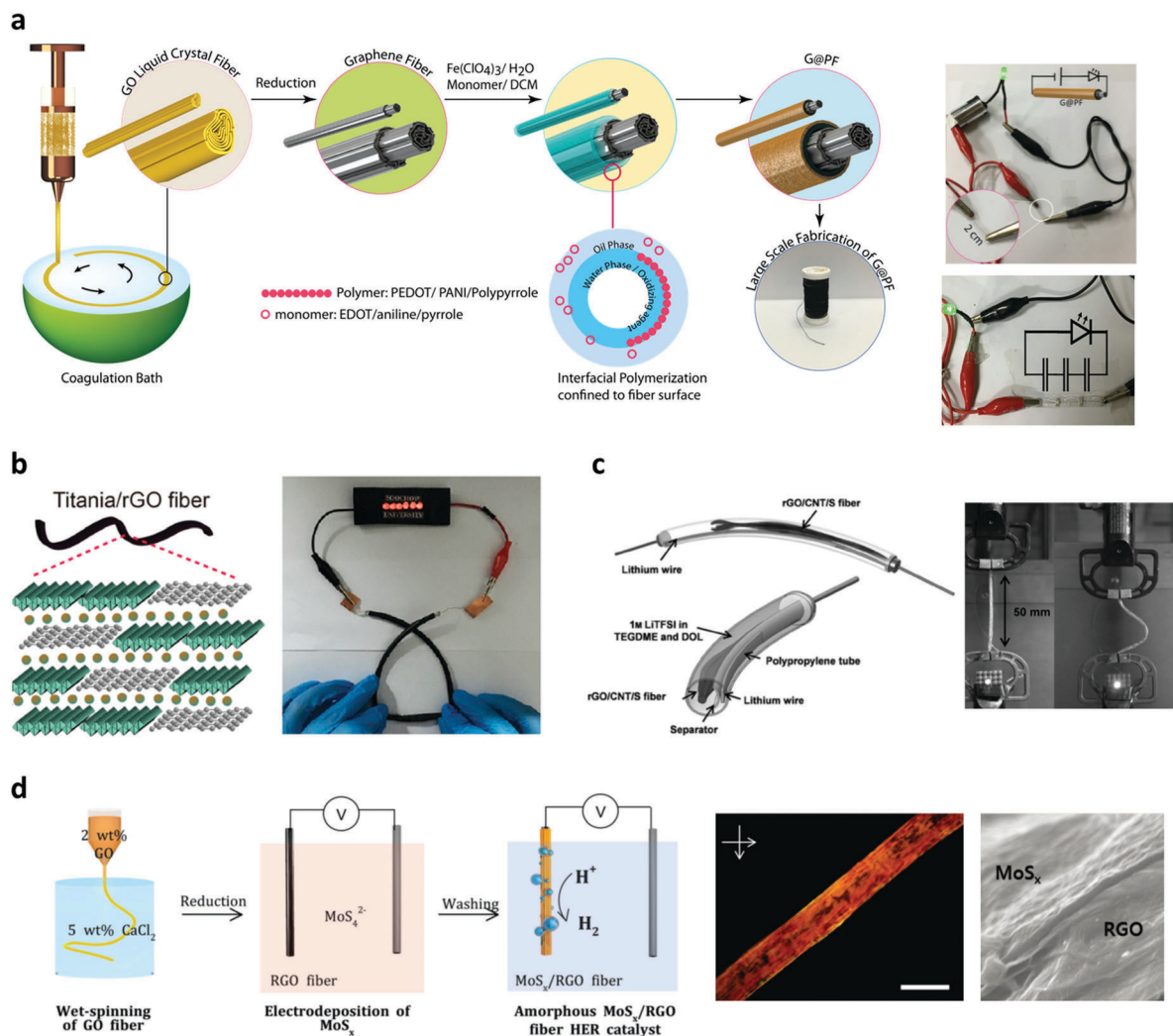


Fig. 16 Graphene fiber-based energy storage/electrocatalytic electrodes. (a) Schematic illustration displaying the fabrication steps for graphene/polymer core–shell fibers; reproduced from ref. 16 with permission from the American Chemical Society, copyright 2017. (b) Schematic illustration of the fabrication process for titania/rGO hybrid fiber for fiber-shaped batteries (left) and lighting up 6 LED lamps with a 30 cm fiber-shaped battery (right); reproduced from ref. 129 with permission from the American Chemical Society, copyright 2017. (c) Schematic of a cable lithium–sulfur battery and cross-sectional view of the cable lithium–sulfur battery components; reproduced from ref. 130 with permission from John Wiley and Sons, copyright 2016. (d) Schematic illustration of the fabrication process of amorphous MoS_x /RGO hybrid fiber through a wet-spinning and electrodeposition method (left). Polarized microscope image of a wet-spun GO hydrogel fiber (middle) and SEM image of MoS_x film deposited on RGO fiber (right); reproduced from ref. 15 with permission from John Wiley and Sons, copyright 2017.

(capacity retention of 70% after 200 cycles). Fiber-shaped GO/CNT/sulfur composite cathodes for lithium–sulfur batteries were prepared using a nematic phase LC in GO-dimethylformamide (DMF) (Fig. 16c).¹³⁰ CNT/S composites prepared by a melt diffusion method were mixed with the GO-DMF dispersion. The as-prepared GO/CNT/sulfur spinning dope was then injected into an ethyl acetate coagulation bath. After subsequent drying and chemical reduction by HI vapor, the composite fibers could deliver a high initial capacity of 1255 mA h g^{-1} and areal capacity of $2.49 \text{ mA h cm}^{-2}$ at C/20.

Recently, we reported rGO-fiber-based electrocatalysts incorporated with amorphous molybdenum sulfide (MoS_x) (Fig. 16d).¹⁵ Nanoscale-thick amorphous MoS_x layers, of which unsaturated defect sites have been proven to be efficient as hydrogen evolution reaction (HER) catalytic sites, were electrochemically deposited over

the graphene fiber surface. The MoS_x /rGO nanocomposite fibers exhibited excellent HER catalytic activity and stability. The simple strategy to fabricate multifunctional graphene-based fibers could be expanded to prepare various nanocomposite materials to greatly broaden the spectrum of applications of graphene with fibers, such as energy storage/conversion. It is noteworthy that together with GOLC, the recent discovery of LC nematic alignment of Mexene has opened up remarkable opportunities in energy storage applications as well.¹⁸⁵

4.6. Optical applications: optical switching and photonic crystals

Optical-switching devices are one of the representative applications utilizing GOLC. The high sensitivity of nematic phase GOLC to

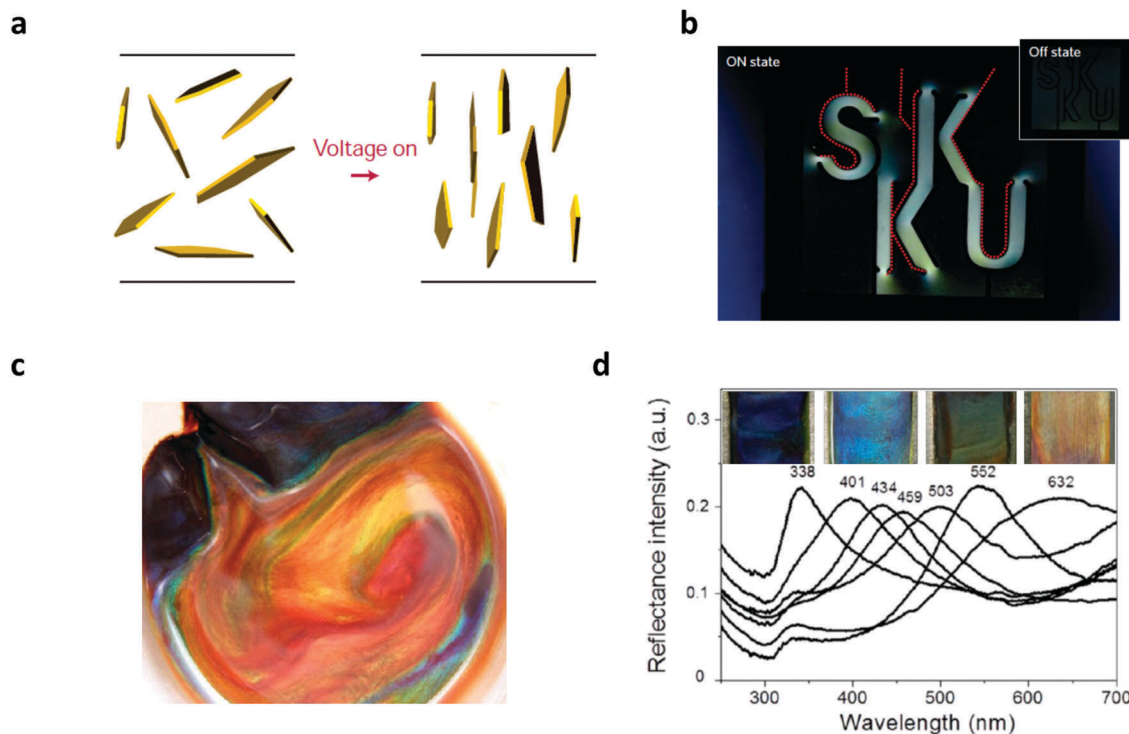


Fig. 17 Optical applications of GOLCs. (a) The electric-field-induced orientation of an isotropic GO dispersion of low concentration (0.05 vol%); reproduced from ref. 12 with permission from Springer Nature, copyright 2014, (b) field-on and field-off states of an electro-optic GOLC device with simple macroscopic wire electrodes; reproduced from ref. 13 with permission from Springer Nature, copyright 2014. (c) Iridescent color of large-sized GO gel photonic crystals. (d) Optical reflectance spectra and photographs of large-sized GO dispersions of different structural colors. From left to right, the weight fractions of large-sized GO were 0.75, 0.67, 0.51, and 0.36 wt%, respectively; reproduced from ref. 131 with permission from the American Chemical Society, copyright 2014.

external stimulation is effectively exploited for use in electro-optic devices. It is possible to control the alignment direction of a GOLC by adjusting the magnitude and direction of the electric field (Fig. 17a).¹² GOCLs have shown large polarizability anisotropy and the Onsager excluded-volume effect, leading to high Kerr coefficients, which were three orders of magnitude higher than the highest value recorded thus far. The extremely high Kerr coefficient enabled fabrication of an optical-switching device with wire-type electrodes under an applied voltage of 20 V on the electrodes (Fig. 17b).¹³

Color-tunable photonic crystals based on large-sized amphiphilic GO in aqueous dispersion were demonstrated by Sue *et al.* via a simple colloidal self-assembly approach. A large GO aqueous dispersion in gel form showed brilliant structural colors under the irradiation of white light (Fig. 17c).¹³¹ This is ascribed to Bragg reflection of long-range order of a large GOLC. Interestingly, the wavelength of light, *i.e.* color reflection, by the GO photonic crystal dispersion was adjustable from violet to red with GO concentration (Fig. 17d). The width of the reflection peak was widened at a low GO concentration. Along with the GO concentration, a relatively narrow reflection peak was observed due to the “excluded-volume” effect based on Platz’s theory.

4.7. Other applications: sensors, self-power devices and transistors

Nowadays, the application spectrum of GOLC-based graphene materials is continuously growing. In this section, diversified

applications of GOLC-based materials are briefly introduced, and how the LC properties are exploited for those applications are then briefly discussed. Flexible, bendable and wearable fiber-shaped materials are very suitable forms for wearable sensors and for real-time healthcare monitoring. Choi *et al.* recently reported a unique humidity sensing layer composed of N-doped reduced graphene oxide (NrGO) fiber on a colorless polyimide film (Fig. 18a and b).¹³² GOLC fibers were synthesized by the solution assembly of large GO sheets in LC states. After thermal N-doping under a H₂ (4%)/N₂ (96%) mixture gas, Pt nanoparticles of 2 nm were tightly anchored at the fiber surface as water dissociation catalysts. The rGO-based fibers exhibited effective water sensing in the range of 6.1–66.4% relative humidity (RH). The sensitivity to water molecules of the Pt anchored N-doped rGO fibers (Pt/NrGO) showed a 1.36-fold higher sensitivity (4.51%) at 66.4% RH, compared with the sensitivity (3.53% at 66.4% RH) of pure NrGO fiber. The real-time and portable humidity sensing characteristics were successfully demonstrated toward exhaled breath using a Pt–NrGO fiber integrated on a portable sensing module. Such Pt–NrGO fibers with high sensitivity and a wide range of humidity detection levels offer a new sensing platform for wearable humidity sensors. Recently, a self-powered wearable graphene fiber has been reported based on a moisture-electric energy transformation (MEET) process to achieve highly efficient energy harvesting from external environments, which represents a new type of

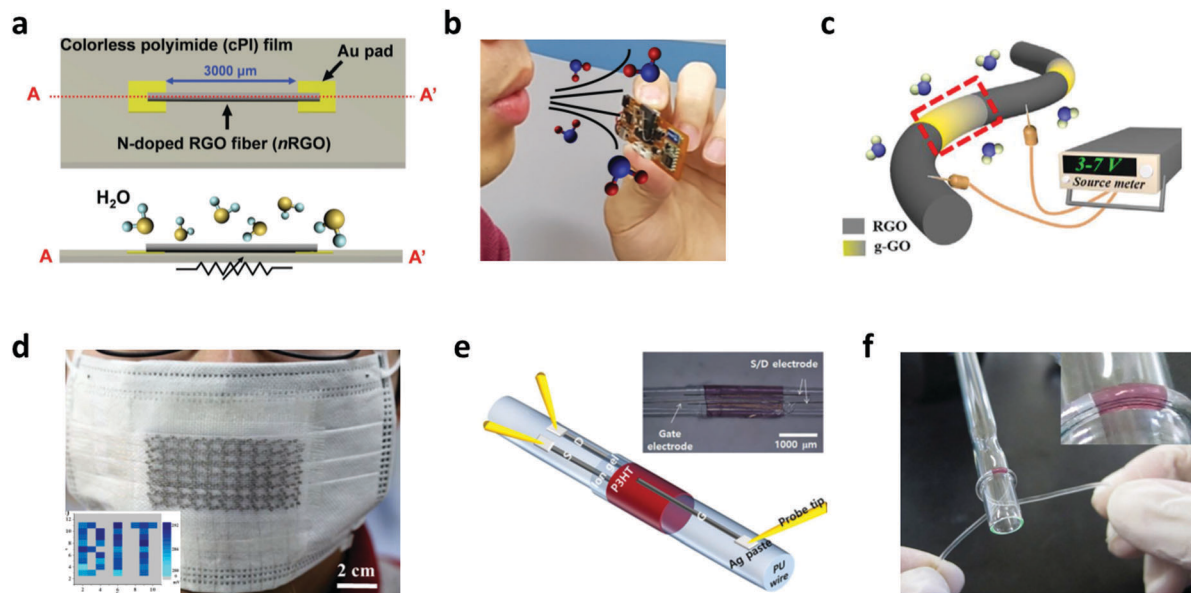


Fig. 18 Diversified application field of GOLCs. (a) Schematic illustration of humidity sensors based on a reduced and nitrogen-doped graphene oxide (NrGO) fiber. (b) Real breath injection into the Pt-NrGO fiber sensor integrated with the portable breath humidity sensing module; reproduced from ref. 132 with permission from John Wiley and Sons, copyright 2018. (c) Schematic illustration of the operation of graphene fiber power generators by moisture-electric energy transformation. (d) The device containing 136 graphene fiber power generator units attached on a mask. Inset images express the electronic label: voltage outputs of all the graphene fiber power generator units. The voltage outputs are testing after a deep breath ($\Delta RH = 35\%$); reproduced from ref. 133 with permission from Elsevier, copyright 2017. (e) Schematic illustration and photograph of a fiber-type transistor based on graphene/Ag hybrid fiber electrodes. (f) Photographs of a fiber-shaped transistor bent by a glass rod of 2 mm radius, reproduced from ref. 134 with permission from Scientific Reports, copyright 2015 (<http://creativecommons.org/licenses/by/4.0/>).

power resource.¹³³ The MEET mechanism is based on the hydration of functional materials with gradient distributed ionizable groups, where free ions are released by water-molecules-triggered ionization. The migration of free ions driven by the concentration gradient induced the generation of a voltage and current. The hydroelectric power generation from the MEET process is directly related to the hydrophilicity, permeability and ionic conductivity of functional materials. Liang *et al.* generated gradient distributed ionizable groups in wet-spun GO fibers by using well-controlled regio-selective laser irradiation to form an alternative distribution of RGO and GO (Fig. 18c), yielding finally graphene fiber power generators for energy harvesting from environmental moisture. A single graphene fiber power generator was able to generate a high voltage output of *ca.* 0.4 V upon variation of the environmental relative humidity (ΔRH). Moreover, integration of the moisture-induced self-powered fiber into flexible textiles was realized for an information storage/expression based on the breath-activated electronic labels of graphene fiber power generators (Fig. 18d).

A fiber-shaped and planar transistor has also been demonstrated based on conductive and flexible graphene/Ag hybrid fibers (Fig. 18e and f).¹³⁴ Wet-spun and HI-reduced rGO fibers were incorporated with Ag nanoparticles. The graphene/Ag hybrid fibers exhibited an outstanding electrical conductivity of $15\,800\text{ S cm}^{-1}$ and thereby have been employed as source, drain and gate electrodes for ion gel-gated planar transistors. The graphene/Ag hybrid fiber was embedded onto conventional monofilaments for fiber-shaped transistor devices. The unique

fiber-shaped switching devices showed excellent flexibility, high electrical performance ($\mu_{\text{th}} = 15.6\text{ cm}^2\text{ V}^{-1}\text{ s}^{-1}$, $I_{\text{on}}/I_{\text{off}} > 10^4$), and stable operation after 1000 cycles of bending tests and exposure to ambient conditions for 30 days.

5. Conclusions and outlook

GO-based materials have suffered from notorious processability issues, arising from the extremely large shape anisotropy and wide polydispersity of GO sheets. Clearly, GOLC offers unprecedented opportunities for the precise control of GO sheets to attain highly organized functional assembled structures. A number of desired architectures with various geometrical dimensions, ranging from one- to full three-dimensional can be generated and further transformed into highly functional structures after an appropriate chemical/thermal reduction and chemical modification/doping. Motivated by these unique advantages, GOLCs have advanced remarkably among many different 2D materials in a relatively short time span since our first discovery. The ideal combination of cost-effective scalable synthesis, solvent dispersibility, chemically active surface functionalities, and the possibility for further chemical modification/doping has fueled such an exceedingly rapid evolution. This review was structured in such a way to provide readers clear and comprehensive insights into all the different aspects of GOLC research, including the structure, properties, synthesis, and applications of GOLCs. Notably, different parameters to be optimized for GOLC formation and

general characterization methods for GOLC have been particularly elaborated for achieving a fundamental grasp of GOLCs. The unique blending of outstanding properties of graphene-based materials with the spontaneous molecular ordering and fluidity of LCs will undoubtedly ensure a thrilling and prosperous future for GOLCs.

Despite the unusually rapid advances made in the fundamental research and potential applications of GOLCs, this field is still in its early stage with many critical issues, particularly in the synthesis and potential properties of GOLCs, which can even cause bottlenecks to the eventual commercial success. For instance, as aforementioned, many parameters, such as the pH, ionic strength, degree of surface functionality, and aspect ratio of GO sheets, strongly influence the formation and stability of GOLCs. A standardized method to control these delicately interrelated parameters upon the synthesis of GO is still a highly demanded and open challenge. Moreover, currently available synthetic methodologies, even though straightforward and scalable, consistently struggle to address the growing environmental and human safety concerns caused by the inevitable use of strong acids and oxidants. Noticeable progress has been made, including the electrochemical oxidation reported recently, but still tends to suffer from the substantial use of strong acids.⁵⁵ A truly environment benign and scalable method for the synthesis of GO is yet to be identified. A minimal use of harsh oxidants is also critical in order to relieve the formidable burden for the post-synthetic purification of GO, which can significantly influence its LC phase formation and the final material properties derived from the LC phase. Another major challenge is how to control the polydispersity of GO sheets, which can significantly influence the uniformity and reliability of graphene-based materials and structures derived from the GOLC phase. Gravity-induced spontaneous selection of the high-density LC phase with large GO sheets has been successfully practiced so far; however, this is relatively time consuming. Recently introduced rapid electrophoretic size selection seems interesting but should be explored further to achieve a reliable methodology.⁸³ Further progress in GOLC research is certainly anticipated to hinge on the development of synthetic methods, where the size, shape and degree of functionalities at GO sheets can be precisely controlled. Surprisingly, due to the inherent hygroscopic nature of GO, the exact chemical and physical structures of GO have not been fully elucidated yet. These remains a significant uncertainty in the structure–property correlations, which demands more rigorous research from experimental and theoretical points of view.

As foreshadowed in the earlier research, the recovery of the original superior characteristics of graphene, such as high electrical/thermal conductivity and tensile strength, has not yet been realized fully by the current reduction and doping methods for GOLCs. Improvement in the pre-existing reduction methods to impose fewer defects and achieve a higher crystallinity in the graphene crystal lattice are tremendously challenging yet critically imperative. Indeed, this is a serious practical issue for any kind of material processing based on chemically modified graphene-based materials, such as GO. Currently, typical chemical treatments with hydrazine or HI, or high temperature treatment methods, are widely employed for this purpose.

Unfortunately, their high processing costs, principally arising from the toxicity of reductants and high temperature chamber control, represent crucial limitations. Despite the high-cost processing, nonetheless, the recovery of the original graphitic structure and properties is still far from at a desired level. Energy efficient, environmentally benign but highly effective reduction and doping methods for GO need to be further investigated. In this regard, recent research efforts for the radiation-induced chemical modification of graphene-based materials look promising but require further improvements in various aspects.

It is well recognized that owing to the large shape anisotropy and broad polydispersity, GOLCs show a nematic phase in general with a noticeably broad isotropic to nematic phase transition range. Meanwhile, the remarkable but still controversial observation of a chiral and lamellar LC phase at a high GOLC concentration may propose a novel future research direction; for instance, investigation of the dynamic and equilibrium properties of GOLCs with chiral biological systems, such as DNA or viruses.¹³⁵ Motivated from the generic miscibility of the identical LC phases, the biocompatibility of GOLC with biological LC systems is an interesting subject. In the near future, it might be possible to design novel reconfigurable graphene-based biological hybrid materials whose chirality can be controlled by targeted stimuli. In this regard, modeling studies based on a simulation of the molecular behaviors of LCs can be implemented to understand and predict the interesting properties of GOLCs and their assembled structures to some extent. Such a fundamental research effort may also facilitate how to understand the delicate anchoring and assembly behaviors of GOLCs under the interplay among multiple external stimuli, such as a flow field, electrical/magnet field, or within the physical confinement enforced by the complicated processing geometry.^{136,137}

Overall, tackling all the aforementioned challenges inevitably requires global synergic efforts, both from the LC community and the graphene community to ensure robust innovative growth in this field. Improving the basic knowledge with the support from the two complementary disciplines can potentially lighten unforeseen possibilities in the inherently interdisciplinary subject of GOLC research in the near future. It is noteworthy that the lessons learned from the frontier GOLC research should also be useful to all 2D material research in general. We believe this review will contribute to this wide vision to expand the boundaries of GOLC research and to open up future research directions.

Conflicts of interest

There are no conflicts of interest to declare.

Acknowledgements

All authors acknowledge the financial support from the National Creative Research Initiative (CRI) Center for Multi-Dimensional Directed Nanoscale Assembly (2015R1A3A2033061)

and Nanomaterial Technology Development Program through the National Research Foundation of Korea (NRF) funded by the Ministry of Science, ICT and Future Planning (NRF-2016M3A7B4905609). T. H. H. acknowledge funding from Basic Science Research Program (2017R1A2B4010771) of the National Research Foundation of Korea also.

Notes and references

- J. E. Kim, Master thesis, Korea Advanced Institute of Science and Technology, 2009, pp. 1–58.
- J. E. Kim, T. H. Han, S. H. Lee, J. Y. Kim, C. W. Ahn, J. M. Yun and S. O. Kim, *Angew. Chem., Int. Ed.*, 2011, **50**, 3043–3047.
- S. O. Kim, J. E. Kim, T. H. Han, S. H. Lee and J. Y. Kim, Korea Advanced Institute of Science and Technology, Korea Patent Filing date 08/03/2010, Registration number: KR10-1210513.
- S. O. Kim, J. E. Kim, T. H. Han, S. H. Lee and J. Y. Kim, Korea Advanced Institute of Science and Technology, USA Patent filing date 22/10/2010, Registration number: 08449791.
- Z. Xu and C. Gao, *ACS Nano*, 2011, **5**, 2908–2915.
- Z. Xu and C. Gao, *Nat. Commun.*, 2011, **2**, 571.
- F. Guo, F. Kim, T. H. Han, V. B. Shenoy, J. Huang and R. H. Hurt, *ACS Nano*, 2011, **5**, 8019–8025.
- R. Jalili, S. H. Aboutalebi, D. Esrafilzadeh, K. Konstantinov, S. E. Moulton, J. M. Razal and G. G. Wallace, *ACS Nano*, 2013, **7**, 3981–3990.
- R. Jalili, S. H. Aboutalebi, D. Esrafilzadeh, K. Konstantinov, J. M. Razal, S. E. Moulton and G. G. Wallace, *Mater. Horiz.*, 2014, **1**, 87–91.
- B. Konkena and S. Vasudevan, *J. Phys. Chem. C*, 2014, **118**, 21706–21713.
- K. E. Lee, J. E. Kim, U. N. Maiti, J. Lim, J. O. Hwang, J. Shim, J. J. Oh, T. Yun and S. O. Kim, *ACS Nano*, 2014, **8**, 9073–9080.
- J. Y. Kim and S. O. Kim, *Nat. Mater.*, 2014, **13**, 325–326.
- T.-Z. Shen, S.-H. Hong and J.-K. Song, *Nat. Mater.*, 2014, **13**, 394–399.
- B. Yao, J. Chen, L. Huang, Q. Zhou and G. Shi, *Adv. Mater.*, 2016, **28**, 1623–1629.
- K. E. Lee, S. P. Sasikala, H. J. Lee, G. Y. Lee, S. H. Koo, T. Yun, H. J. Jung, I. Kim and S. O. Kim, *Part. Part. Syst. Charact.*, 2017, **34**, 1600375.
- S. Padmajan Sasikala, K. E. Lee, J. Lim, H. J. Lee, S. H. Koo, I. H. Kim, H. J. Jung and S. O. Kim, *ACS Nano*, 2017, **11**, 9424–9434.
- R. Narayan, J. E. Kim, J. Y. Kim, K. E. Lee and S. O. Kim, *Adv. Mater.*, 2016, **28**, 3045–3068.
- F. Lin, X. Tong, Y. Wang, J. Bao and Z. M. Wang, *Nanoscale Res. Lett.*, 2015, **10**, 435.
- M. Kumar, A. Gowda and S. Kumar, *Part. Part. Syst. Charact.*, 2017, **34**, 1700003.
- J. Zhang, S. Seyedin, Z. Gu, N. Salim, X. Wang and J. M. Razal, *Part. Part. Syst. Charact.*, 2017, **34**, 1600396.
- F. Reinitzer, *Monatsh. Chem.*, 1888, **9**, 421–441.
- P.-G. d. Gennes, *The Physics of Liquid Crystals*, Clarendon Press, 1974.
- J. Prost, *The Physics of Liquid Crystals*, Oxford University Press, 1995.
- P. Popov, L. W. Honaker, M. Mirheydari, E. K. Mann and A. Jáklí, *Sci. Rep.*, 2017, **7**, 1603.
- S. Ermakov, A. Beletskii, O. Eismont and V. Nikolaev, *Liquid Crystals in Biotribology*, Springer, 2016, pp. 37–56.
- S. Chandrasekhar, *Liq. Cryst.*, 1993, **14**, 3–14.
- B. G. Kulichikhin, *Liquid-Crystal Polymers*, Springer, 1993, pp. 339–382.
- G. H. Brown, J. W. Dome and V. D. Neff, *Crit. Rev. Solid State Mater. Sci.*, 1970, **1**, 303–379.
- G. Brown, *Liquid Crystals and Biological Structures*, Elsevier, 2012.
- M. Hird, *Chem. Soc. Rev.*, 2007, **36**, 2070–2095.
- H. K. Bisoyi and S. Kumar, *Chem. Soc. Rev.*, 2011, **40**, 306–319.
- Y. Liu, Z. Xu, W. Gao, Z. Cheng and C. Gao, *Adv. Mater.*, 2017, **29**, 1606794.
- I. Potočová, P. Kopčanský, M. Koneracká, L. Tomčo, M. Timko, J. Jadzyn and G. Czechowski, *J. Magn. Magn. Mater.*, 2002, **252**, 150–152.
- O. Stamatoiu, J. Mirzaei, X. Feng and T. Hegmann, *Liquid Crystals*, Springer, 2011, pp. 331–393.
- M.-H. Lin, H.-Y. Chen and S. Gwo, *J. Am. Chem. Soc.*, 2010, **132**, 11259–11263.
- T. Hegmann, H. Qi and V. M. Marx, *J. Inorg. Organomet. Polym. Mater.*, 2007, **17**, 483–508.
- H. K. Bisoyi and Q. Li, *Anisotropic Nanomaterials*, Springer, 2015, pp. 209–240.
- S. H. Aboutalebi, M. M. Gudarzi, Q. B. Zheng and J. K. Kim, *Adv. Funct. Mater.*, 2011, **21**, 2978–2988.
- V. A. Davis, A. N. G. Parra-Vasquez, M. J. Green, P. K. Rai, N. Behabtu, V. Prieto, R. D. Booker, J. Schmidt, E. Kesselman, W. Zhou, H. Fan, W. W. Adams, R. H. Hauge, J. E. Fischer, Y. Cohen, Y. Talmon, R. E. Smalley and M. Pasquali, *Nat. Nanotechnol.*, 2009, **4**, 830.
- N. Behabtu, J. R. Lomeda, M. J. Green, A. L. Higginbotham, A. Sinitskii, D. V. Kosynkin, D. Tsentalovich, A. N. G. Parra-Vasquez, J. Schmidt, E. Kesselman, Y. Cohen, Y. Talmon, J. M. Tour and M. Pasquali, *Nat. Nanotechnol.*, 2010, **5**, 406.
- C. Zamora-Ledezma, N. Puech, C. Zakri, E. Grelet, S. E. Moulton, G. G. Wallace, S. Gambhir, C. Blanc, E. Anglaret and P. Poulin, *J. Phys. Lett.*, 2012, **3**, 2425–2430.
- L. Tong, W. Qi, M. Wang, R. Huang, R. Su and Z. He, *Chem. Commun.*, 2014, **50**, 7776–7779.
- R. Jalili, S. Aminorroaya-Yamini, T. M. Benedetti, S. H. Aboutalebi, Y. Chao, G. G. Wallace and D. L. Officer, *Nanoscale*, 2016, **8**, 16862–16867.
- B. C. Brodie, *Philos. Trans. R. Soc. London*, 1859, **149**, 249–259.
- S. Stankovich, D. A. Dikin, G. H. B. Dommett, K. M. Kohlhaas, E. J. Zimney, E. A. Stach, R. D. Piner, S. T. Nguyen and R. S. Ruoff, *Nature*, 2006, **442**, 282.

- 46 D. A. Dikin, S. Stankovich, E. J. Zimney, R. D. Piner, G. H. Dommett, G. Evmenenko, S. T. Nguyen and R. S. Ruoff, *Nature*, 2007, **448**, 457–460.
- 47 S. Stankovich, D. A. Dikin, R. D. Piner, K. A. Kohlhaas, A. Kleinhammes, Y. Jia, Y. Wu, S. T. Nguyen and R. S. Ruoff, *Carbon*, 2007, **45**, 1558–1565.
- 48 N. I. Kovtyukhova, P. J. Ollivier, B. R. Martin, T. E. Mallouk, S. A. Chizhik, E. V. Buzaneva and A. D. Gorchinskiy, *Chem. Mater.*, 1999, **11**, 771–778.
- 49 W. S. Hummers and R. E. Offeman, *J. Am. Chem. Soc.*, 1958, **80**, 1339.
- 50 D. C. Marcano, D. V. Kosynkin, J. M. Berlin, A. Sinitskii, Z. Sun, A. Slesarev, L. B. Alemany, W. Lu and J. M. Tour, *ACS Nano*, 2010, **4**, 4806–4814.
- 51 J. Zhao, S. Pei, W. Ren, L. Gao and H.-M. Cheng, *ACS Nano*, 2010, **4**, 5245–5252.
- 52 T. Soltani and B.-K. Lee, *Ultrason. Sonochem.*, 2017, **38**, 693–703.
- 53 J. H. Kang, T. Kim, J. Choi, J. Park, Y. S. Kim, M. S. Chang, H. Jung, K. T. Park, S. J. Yang and C. R. Park, *Chem. Mater.*, 2016, **28**, 756–764.
- 54 L. Peng, Z. Xu, Z. Liu, Y. Wei, H. Sun, Z. Li, X. Zhao and C. Gao, *Nat. Commun.*, 2015, **6**, 5716.
- 55 S. Pei, Q. Wei, K. Huang, H.-M. Cheng and W. Ren, *Nat. Commun.*, 2018, **9**, 145.
- 56 D. Chen, H. Feng and J. Li, *Chem. Rev.*, 2012, **112**, 6027–6053.
- 57 H. He, J. Klinowski, M. Forster and A. Lerf, *Chem. Phys. Lett.*, 1998, **287**, 53–56.
- 58 A. Lerf, H. He, M. Forster and J. Klinowski, *J. Phys. Chem. B*, 1998, **102**, 4477–4482.
- 59 W. Gao, L. B. Alemany, L. Ci and P. M. Ajayan, *Nat. Chem.*, 2009, **1**, 403.
- 60 A. M. Dimiev and J. M. Tour, *ACS Nano*, 2014, **8**, 3060–3068.
- 61 J. I. Paredes, S. Villar-Rodil, A. Martínez-Alonso and J. M. D. Tascón, *Langmuir*, 2008, **24**, 10560–10564.
- 62 Z.-S. Wu, W. Ren, L. Gao, B. Liu, C. Jiang and H.-M. Cheng, *Carbon*, 2009, **47**, 493–499.
- 63 L. Zhang, J. Liang, Y. Huang, Y. Ma, Y. Wang and Y. Chen, *Carbon*, 2009, **47**, 3365–3368.
- 64 S. Pan and I. A. Aksay, *ACS Nano*, 2011, **5**, 4073–4083.
- 65 E. M. Deemer, P. K. Paul, F. S. Manciu, C. E. Botez, D. R. Hodges, Z. Landis, T. Akter, E. Castro and R. R. Chianelli, *Mater. Sci. Eng., C*, 2017, **224**, 150–157.
- 66 Z.-B. Liu, Y.-F. Xu, X.-Y. Zhang, X.-L. Zhang, Y.-S. Chen and J.-G. Tian, *J. Phys. Chem. B*, 2009, **113**, 9681–9686.
- 67 S. Stankovich, R. D. Piner, S. T. Nguyen and R. S. Ruoff, *Carbon*, 2006, **44**, 3342–3347.
- 68 K. A. Mkhoyan, A. W. Contryman, J. Silcox, D. A. Stewart, G. Eda, C. Mattevi, S. Miller and M. Chhowalla, *Nano Lett.*, 2009, **9**, 1058–1063.
- 69 K. Erickson, R. Erni, Z. Lee, N. Alem, W. Gannett and A. Zettl, *Adv. Mater.*, 2010, **22**, 4467–4472.
- 70 S. H. Dave, C. Gong, A. W. Robertson, J. H. Warner and J. C. Grossman, *ACS Nano*, 2016, **10**, 7515–7522.
- 71 R. J. W. E. Lahaye, H. K. Jeong, C. Y. Park and Y. H. Lee, *Phys. Rev. B: Condens. Matter Mater. Phys.*, 2009, **79**, 125435.
- 72 V. Gupta, N. Sharma, U. Singh, M. Arif and A. Singh, *Optik*, 2017, **143**, 115–124.
- 73 M. M. Gudarzi, M. H. M. Moghadam and F. Sharif, *Carbon*, 2013, **64**, 403–415.
- 74 A. O'Neill, U. Khan, P. N. Nirmalraj, J. Boland and J. N. Coleman, *J. Phys. Chem. C*, 2011, **115**, 5422–5428.
- 75 I. W. Hamley, *Introduction to Soft Matter: Polymer Colloids, Amphiphiles & Liquid crystal*, Wiley, 2000.
- 76 C.-J. Shih, S. Lin, R. Sharma, M. S. Strano and D. Blankschtein, *Langmuir*, 2012, **28**, 235–241.
- 77 M. M. Gudarzi, *Langmuir*, 2016, **32**, 5058–5068.
- 78 H. Tang, D. Liu, Y. Zhao, X. Yang, J. Lu and F. Cui, *J. Phys. Chem. C*, 2015, **119**, 26712–26718.
- 79 Y. Jin, Z. Xu, Y. Guo and X. Yang, *J. Phys. Chem. C*, 2018, **122**, 4063–4072.
- 80 P. Bansal, A. S. Panwar and D. Bahadur, *J. Phys. Chem. C*, 2017, **121**, 9847–9859.
- 81 L. Onsager, *Ann. N. Y. Acad. Sci.*, 1949, **51**, 627–659.
- 82 Z. Liu, Z. Xu, X. Hu and C. Gao, *Macromolecules*, 2013, **46**, 6931–6941.
- 83 S. H. Hong, T. Z. Shen, B. Lee and J. K. Song, *Part. Part. Syst. Charact.*, 2017, **34**, 1600344.
- 84 A. Shundo, K. Hori, D. P. Penaloza, Y. Matsumoto, Y. Okumura, H. Kikuchi, K. E. Lee, S. O. Kim and K. Tanaka, *Phys. Chem. Chem. Phys.*, 2016, **18**, 22399–22406.
- 85 R. Tkacz, R. Oldenbourg, S. B. Mehta, M. Miansari, A. Verma and M. Majumder, *Chem. Commun.*, 2014, **50**, 6668–6671.
- 86 X. Fan, W. Peng, Y. Li, X. Li, S. Wang, G. Zhang and F. Zhang, *Adv. Mater.*, 2008, **20**, 4490–4493.
- 87 R. Tkacz, M. J. Abedin, P. Sheath, S. B. Mehta, A. Verma, R. Oldenbourg and M. Majumder, *Part. Part. Syst. Charact.*, 2017, **34**, 1600391.
- 88 X. Zhao, Z. Xu, Y. Xie, B. Zheng, L. Kou and C. Gao, *Langmuir*, 2014, **30**, 3715–3722.
- 89 J. Yuan, A. Luna, W. Neri, C. Zakri, T. Schilling, A. Colin and P. Poulin, *Nat. Commun.*, 2015, **6**, 8700.
- 90 X. Zhao, Z. Xu, B. Zheng and C. Gao, *Sci. Rep.*, 2013, **3**, 3164.
- 91 M. Wang, Y. Li and H. Yokoyama, *Nat. Commun.*, 2017, **8**, 388.
- 92 B. Senyuk, N. Behabtu, B. G. Pacheco, T. Lee, G. Ceriotti, J. M. Tour, M. Pasquali and I. I. Smalyukh, *ACS Nano*, 2012, **6**, 8060–8066.
- 93 M. R. Alcantara and J. Vanin, *Colloids Surf., A*, 1995, **97**, 151–156.
- 94 X. Yang, C. Guo, L. Ji, Y. Li and Y. Tu, *Langmuir*, 2013, **29**, 8103–8107.
- 95 S.-H. Hong, T.-Z. Shen and J.-K. Song, *Liq. Cryst.*, 2015, **42**, 261–269.
- 96 P. Kumar, U. N. Maiti, K. E. Lee and S. O. Kim, *Carbon*, 2014, **80**, 453–461.
- 97 S. Naficy, R. Jalili, S. H. Aboutalebi, R. A. Gorkin Iii, K. Konstantinov, P. C. Innis, G. M. Spinks, P. Poulin and G. G. Wallace, *Mater. Horiz.*, 2014, **1**, 326–331.
- 98 P. Poulin, R. Jalili, W. Neri, F. Nallet, T. Divoux, A. Colin, S. H. Aboutalebi, G. Wallace and C. Zakri, *Proc. Natl. Acad. Sci. U. S. A.*, 2016, **113**, 11088.

- 99 X. Hu, Z. Xu and C. Gao, *Sci. Rep.*, 2012, **2**, 767.
- 100 L. Liao, Y.-C. Lin, M. Bao, R. Cheng, J. Bai, Y. Liu, Y. Qu, K. L. Wang, Y. Huang and X. Duan, *Nature*, 2010, **467**, 305.
- 101 L. Qu, Y. Liu, J.-B. Baek and L. Dai, *ACS Nano*, 2010, **4**, 1321–1326.
- 102 T. Ramanathan, A. Abdala, S. Stankovich, D. Dikin, M. Herrera-Alonso, R. Piner, D. Adamson, H. Schniepp, X. Chen and R. Ruoff, *Nat. Nanotechnol.*, 2008, **3**, 327.
- 103 W. Gao, *Graphene oxide*, Springer, 2015, pp. 61–95.
- 104 D. Li, M. B. Müller, S. Gilje, R. B. Kaner and G. G. Wallace, *Nat. Nanotechnol.*, 2008, **3**, 101.
- 105 M. D. Stoller, S. Park, Y. Zhu, J. An and R. S. Ruoff, *Nano Lett.*, 2008, **8**, 3498–3502.
- 106 H. A. Becerril, J. Mao, Z. Liu, R. M. Stoltenberg, Z. Bao and Y. Chen, *ACS Nano*, 2008, **2**, 463–470.
- 107 S. Park, K.-S. Lee, G. Bozoklu, W. Cai, S. T. Nguyen and R. S. Ruoff, *ACS Nano*, 2008, **2**, 572–578.
- 108 V. Chabot, D. Higgins, A. Yu, X. Xiao, Z. Chen and J. Zhang, *Energy Environ. Sci.*, 2014, **7**, 1564–1596.
- 109 Z. Xu, H. Sun, X. Zhao and C. Gao, *Adv. Mater.*, 2013, **25**, 188–193.
- 110 G. Xin, T. Yao, H. Sun, S. M. Scott, D. Shao, G. Wang and J. Lian, *Science*, 2015, **349**, 1083–1087.
- 111 S. Seyedin, M. S. Romano, A. I. Minett and J. M. Razal, *Sci. Rep.*, 2015, **5**, 14946.
- 112 R. Jalili, S. H. Aboutalebi, D. Esrafilzadeh, R. L. Shepherd, J. Chen, S. Aminorroaya-Yamini, K. Konstantinov, A. I. Minett, J. M. Razal and G. G. Wallace, *Adv. Funct. Mater.*, 2013, **23**, 5345–5354.
- 113 C. Xiang, N. Behabtu, Y. Liu, H. G. Chae, C. C. Young, B. Genorio, D. E. Tsentalovich, C. Zhang, D. V. Kosynkin and J. R. Lomeda, *ACS Nano*, 2013, **7**, 1628–1637.
- 114 L. Chen, Y. He, S. Chai, H. Qiang, F. Chen and Q. Fu, *Nanoscale*, 2013, **5**, 5809–5815.
- 115 S. H. Aboutalebi, R. Jalili, D. Esrafilzadeh, M. Salari, Z. Gholamvand, S. Aminorroaya Yamini, K. Konstantinov, R. L. Shepherd, J. Chen and S. E. Moulton, *ACS Nano*, 2014, **8**, 2456–2466.
- 116 X. Lin, X. Shen, Q. Zheng, N. Yousefi, L. Ye, Y.-W. Mai and J.-K. Kim, *ACS Nano*, 2012, **6**, 10708–10719.
- 117 W. Eom, H. Park, S. H. Noh, K. H. Koh, K. Lee, W. J. Lee and T. H. Han, *Part. Part. Syst. Charact.*, 2017, **34**, 1600401.
- 118 J. O. Hwang, J. S. Park, D. S. Choi, J. Y. Kim, S. H. Lee, K. E. Lee, Y.-H. Kim, M. H. Song, S. Yoo and S. O. Kim, *ACS Nano*, 2011, **6**, 159–167.
- 119 X. Yang, C. Cheng, Y. Wang, L. Qiu and D. Li, *Science*, 2013, **341**, 534–537.
- 120 Z. Liu, Z. Li, Z. Xu, Z. Xia, X. Hu, L. Kou, L. Peng, Y. Wei and C. Gao, *Chem. Mater.*, 2014, **26**, 6786–6795.
- 121 S. Naficy, R. Jalili, S. H. Aboutalebi, R. A. Gorkin Iii, K. Konstantinov, P. C. Innis, G. M. Spinks, P. Poulin and G. G. Wallace, *Mater. Horiz.*, 2014, **1**, 326–331.
- 122 U. N. Maiti, J. Lim, K. E. Lee, W. J. Lee and S. O. Kim, *Adv. Mater.*, 2014, **26**, 615–619.
- 123 Y. Xu, K. Sheng, C. Li and G. Shi, *ACS Nano*, 2010, **4**, 4324–4330.
- 124 Z. Xu, Y. Zhang, P. Li and C. Gao, *ACS Nano*, 2012, **6**, 7103–7113.
- 125 J. Kim, L. J. Cote, F. Kim, W. Yuan, K. R. Shull and J. Huang, *J. Am. Chem. Soc.*, 2010, **132**, 8180–8186.
- 126 K. E. Lee, J. J. Oh, T. Yun and S. O. Kim, *J. Solid State Chem.*, 2015, **224**, 115–119.
- 127 Y. Hu, H. Cheng, F. Zhao, N. Chen, L. Jiang, Z. Feng and L. Qu, *Nanoscale*, 2014, **6**, 6448–6451.
- 128 B. Zheng, T. Huang, L. Kou, X. Zhao, K. Gopalsamy and C. Gao, *J. Mater. Chem. A*, 2014, **2**, 9736–9743.
- 129 T. Hoshide, Y. Zheng, J. Hou, Z. Wang, Q. Li, Z. Zhao, R. Ma, T. Sasaki and F. Geng, *Nano Lett.*, 2017, **17**, 3543–3549.
- 130 W. G. Chong, J.-Q. Huang, Z.-L. Xu, X. Qin, X. Wang and J.-K. Kim, *Adv. Funct. Mater.*, 2017, **27**, 1604815.
- 131 P. Li, M. Wong, X. Zhang, H. Yao, R. Ishige, A. Takahara, M. Miyamoto, R. Nishimura and H.-J. Sue, *ACS Photonics*, 2014, **1**, 79–86.
- 132 S. J. Choi, H. Yu, J. S. Jang, M. H. Kim, S. J. Kim, H. S. Jeong and I. D. Kim, *Small*, 2018, **14**, 1703934.
- 133 Y. Liang, F. Zhao, Z. Cheng, Q. Zhou, H. Shao, L. Jiang and L. Qu, *Nano Energy*, 2017, **32**, 329–335.
- 134 S. S. Yoon, K. E. Lee, H.-J. Cha, D. G. Seong, M.-K. Um, J.-H. Byun, Y. Oh, J. H. Oh, W. Lee and J. U. Lee, *Sci. Rep.*, 2015, **5**, 16366.
- 135 J. Zhang, W. Feng, H. Zhang, Z. Wang, H. A. Calcaterra, B. Yeom, P. A. Hu and N. A. Kotov, *Nat. Commun.*, 2016, **7**, 10701.
- 136 Y. H. Shim, K. E. Lee, T. J. Shin, S. O. Kim and S. Y. Kim, *Mater. Horiz.*, 2017, **4**, 1157–1164.
- 137 F. Guo, A. Mukhopadhyay, B. W. Sheldon and R. H. Hurt, *Adv. Mater.*, 2011, **23**, 508–513.
- 138 I. Langmuir, *J. Chem. Phys.*, 1938, **6**, 873–896.
- 139 J.-C. P. Gabriel, C. Sanchez and P. Davidson, *J. Phys. Chem.*, 1996, **100**, 11139–11143.
- 140 K. Kajiwara, N. Donkai, Y. Hiragi and H. Inagaki, *Macromol. Chem. Phys.*, 1986, **187**, 2883–2893.
- 141 W. W. Emerson, *Nature*, 1956, **178**, 1248.
- 142 L. J. Michot, I. Bihannic, S. Maddi, S. S. Funari, C. Baravian, P. Levitz and P. Davidson, *Proc. Natl. Acad. Sci. U. S. A.*, 2006, **103**, 16101–16104.
- 143 J.-C. P. Gabriel, F. Camerel, B. J. Lemaire, H. Desvaux, P. Davidson and P. Batail, *Nature*, 2001, **413**, 504.
- 144 A. B. D. Brown, S. M. Clarke and A. R. Rennie, *Langmuir*, 1998, **14**, 3129–3132.
- 145 D. Kleshchanok, P. Holmqvist, J.-M. Meijer and H. N. W. Lekkerkerker, *J. Am. Chem. Soc.*, 2012, **134**, 5985–5990.
- 146 A. E. Saunders, A. Ghezlbash, D.-M. Smilgies, M. B. Sigman and B. A. Korgel, *Nano Lett.*, 2006, **6**, 2959–2963.
- 147 T. Paik, D.-K. Ko, T. R. Gordon, V. Doan-Nguyen and C. B. Murray, *ACS Nano*, 2011, **5**, 8322–8330.
- 148 S. Liu, J. Zhang, N. Wang, W. Liu, C. Zhang and D. Sun, *Chem. Mater.*, 2003, **15**, 3240–3241.
- 149 W.-j. Zhou, J. Zhang, T. Xue, D.-d. Zhao and H.-l. Li, *J. Mater. Chem.*, 2008, **18**, 905–910.
- 150 N. R. Jana, L. A. Gearheart, S. O. Obare, C. J. Johnson, K. J. Edler, S. Mann and C. J. Murphy, *J. Mater. Chem.*, 2002, **12**, 2909–2912.

- 151 P. A. Buining and H. N. W. Lekkerkerker, *J. Phys. Chem.*, 1993, **97**, 11510–11516.
- 152 J. Kim, A. De La Cotte, R. Deloncle, S. Archambeau, C. Biver, J. P. Cano, K. Lahlil, J. P. Boilot, E. Grelet and T. Gacoin, *Adv. Funct. Mater.*, 2012, **22**, 4949–4956.
- 153 B. J. Lemaire, P. Davidson, J. Ferré, J. P. Jamet, P. Panine, I. Dozov and J. P. Jolivet, *Phys. Rev. Lett.*, 2002, **88**, 125507.
- 154 L. S. Li and A. P. Alivisatos, *Adv. Mater.*, 2003, **15**, 408–411.
- 155 A. Dessombz, D. Chiche, P. Davidson, P. Panine, C. Chanéac and J.-P. Jolivet, *J. Am. Chem. Soc.*, 2007, **129**, 5904–5909.
- 156 M. Zorn, M. N. Tahir, B. Bergmann, W. Tremel, C. Grigoriadis, G. Floudas and R. Zentel, *Macromol. Rapid Commun.*, 2010, **31**, 1101–1107.
- 157 M. Zorn and R. Zentel, *Macromol. Rapid Commun.*, 2008, **29**, 922–927.
- 158 M. Zorn, S. Meuer, M. N. Tahir, Y. Khalavka, C. Sönnichsen, W. Tremel and R. Zentel, *J. Mater. Chem.*, 2008, **18**, 3050–3058.
- 159 H. Diesselhorst and H. Freundlich, *Z. Phys.*, 1915, **16**, 419–425.
- 160 S. Murali, T. Xu, B. D. Marshall, M. J. Kayatin, K. Pizarro, V. K. Radhakrishnan, D. Nepal and V. A. Davis, *Langmuir*, 2010, **26**, 11176–11183.
- 161 S. Zhang, P. W. Majewski, G. Keskar, L. D. Pfefferle and C. O. Osuji, *Langmuir*, 2011, **27**, 11616–11621.
- 162 W. Song, I. A. Kinloch and A. H. Windle, *Science*, 2003, **302**, 1363.
- 163 V. A. Davis, L. M. Ericson, A. N. G. Parra-Vasquez, H. Fan, Y. Wang, V. Prieto, J. A. Longoria, S. Ramesh, R. K. Saini, C. Kittrell, W. E. Billups, W. W. Adams, R. H. Hauge, R. E. Smalley and M. Pasquali, *Macromolecules*, 2004, **37**, 154–160.
- 164 S. E. Moulton, M. Maugey, P. Poulin and G. G. Wallace, *J. Am. Chem. Soc.*, 2007, **129**, 9452–9457.
- 165 F. C. Bawden, N. W. Pirie, J. D. Bernal and I. Fankuchen, *Nature*, 1936, **138**, 1051.
- 166 T. E. Strzelecka, M. W. Davidson and R. L. Rill, *Nature*, 1988, **331**, 457.
- 167 X. M. Dong, T. Kimura, J.-F. Revol and D. G. Gray, *Langmuir*, 1996, **12**, 2076–2082.
- 168 T. H. Han, J. Kim, J. S. Park, C. B. Park, H. Ihee and S. O. Kim, *Adv. Mater.*, 2007, **19**, 3924–3927.
- 169 C. L. Stevenson, D. B. Bennett and D. Lechuga-Ballesteros, *J. Pharm. Sci.*, 2005, **94**, 1861–1880.
- 170 L. Staudenmaier, *Ber. Dtsch. Chem. Ges.*, 1898, **31**, 1481–1487.
- 171 U. Hofmann and E. König, *Z. Anorg. Allg. Chem.*, 1937, **234**, 311–336.
- 172 M. Hirata, T. Gotou, S. Horiuchi, M. Fujiwara and M. Ohba, *Carbon*, 2004, **42**, 2929–2937.
- 173 P. K. Ang, S. Wang, Q. Bao, J. T. L. Thong and K. P. Loh, *ACS Nano*, 2009, **3**, 3587–3594.
- 174 D. C. Marcano, D. V. Kosynkin, J. M. Berlin, A. Sinitskii, Z. Sun, A. S. Slesarev, L. B. Alemany, W. Lu and J. M. Tour, *ACS Nano*, 2018, **12**, 2078.
- 175 S. Eigler, M. Enzelberger-Heim, S. Grimm, P. Hofmann, W. Kroener, A. Geworski, C. Dotzer, M. Röckert, J. Xiao, C. Papp, O. Lytken, H.-P. Steinrück, P. Müller and A. Hirsch, *Adv. Mater.*, 2013, **25**, 3583–3587.
- 176 H. Yu, B. Zhang, C. Bulin, R. Li and R. Xing, *Sci. Rep.*, 2016, **6**, 36143.
- 177 R. Yuan, J. Yuan, Y. Wu, L. Chen, H. Zhou and J. Chen, *Appl. Surf. Sci.*, 2017, **416**, 868–877.
- 178 H. Freundlich, *Trans. Faraday Soc.*, 1927, **23**, 614–623.
- 179 S. Iijima and T. Ichihashi, *Nature*, 1993, **363**, 603.
- 180 D. S. Bethune, C. H. Kiang, M. S. De Vries, G. Gorman, R. Savoy, J. Vazquez and R. Beyers, *Nature*, 1993, **363**, 605.
- 181 K. S. Novoselov, A. K. Geim, S. V. Morozov, D. Jiang, Y. Zhang, S. V. Dubonos, I. V. Grigorieva and A. A. Firsov, *Science*, 2004, **306**, 666–669.
- 182 J. Y. Oh, J. Park, Y. C. Jeong, J. H. Kim, S. J. Yang and C. R. Park, *Part. Part. Syst. Charact.*, 2017, **34**, 1600383.
- 183 Z. Xu and C. Gao, *Mater. Today*, 2015, **18**, 480–492.
- 184 S. Al-Zangana, M. Iliut, M. Turner, A. Vijayaraghavan and I. Dierking, *2D Mater.*, 2017, **4**, 041004.
- 185 Y. Xia, T. S. Mathis, M. Q. Zhao, B. Anasori, A. Dang, Z. Zhou, H. Cho, Y. Gogotsi and S. Yang, *Nature*, 2018, **557**, 409.